PHYSICAL REVIEW D **94,** 025009 (2016)

Numerical study of chiral plasma instability within the classical statistical field theory approach

P. V. Buividovich[1,*] and M. V. Ulybyshev[1,2,†]

[1]*Institute of Theoretical Physics, University of Regensburg, Universitätsstrasse 31, Regensburg D-93053, Germany*

[2]*Institute for Theoretical Problems of Microphysics, Moscow State University, 119899 Moscow, Russia*

(Received 24 September 2015; published 6 July 2016)

We report on a numerical study of real-time dynamics of electromagnetically interacting chirally imbalanced lattice Dirac fermions within the classical statistical field theory approach. Namely, we perform exact simulations of the real-time quantum evolution of fermionic fields coupled to classical electromagnetic fields, which are in turn coupled to the vacuum expectation value of the fermionic electric current. We use Wilson-Dirac Hamiltonian for fermions, and noncompact action for the gauge field. In general, we observe that the backreaction of fermions on the electromagnetic field prevents the system from acquiring chirality imbalance. In the case of chirality pumping in parallel electric and magnetic fields, the electric field is screened by the produced on-shell fermions and the accumulation of chirality is hence stopped. In the case of evolution with initially present chirality imbalance, axial charge tends to transform to helicity of the electromagnetic field. By performing simulations on large lattices we show that in most cases this decay process is accompanied by the inverse cascade phenomenon, which transfers energy from short-wavelength to long-wavelength electromagnetic fields. In some simulations, however, we observe a very clear signature of inverse cascade for the helical magnetic fields that is not accompanied by the axial charge decay. This suggests that the relation between the inverse cascade and axial charge decay is not as straightforward as predicted by the simplest form of anomalous Maxwell equations.

DOI: 10.1103/PhysRevD.94.025009

I. INTRODUCTION AND BRIEF SUMMARY

Over the past few decades, real-time instability of the system of chiral fermions coupled to dynamical gauge fields has been attracting a lot of attention in various fields of physics, ranging from astrophysics to condensed matter physics. This instability manifests itself in the decay of the initial imbalance between the densities of the left- and right-handed fermions at the expense of the generation of magnetic fields with nonzero magnetic helicity (or, in other words, winding number of magnetic flux lines). In the astrophysical context, the phenomenon of chiral plasma instability is actively discussed as the mechanism responsible for the generation and enhancement of primordial magnetic fields [1–5] as well as for the transfer of magnetic field energy from short to cosmological scales [3,6,7].

In the context of condensed matter physics, it was considered as a mechanism of spontaneous magnetization of topological magnetic insulators [8]. In experiments in which chirally imbalanced Weyl semimetal states are created from Dirac semimetals by applying parallel electric and magnetic fields [9–11] chiral plasma instability might manifest itself in the spontaneous emission of circularly polarized terahertz-range electromagnetic radiation [12].

In heavy-ion collisions, chiral plasma instability might lead to enhanced emission of circularly polarized soft photons [12]. It should be also important for the correct estimate of the lifetimes of chirality imbalance and magnetic fields [13,14]. However, the estimates of [15] suggest that in heavy-ion collisions the volume and the lifetime of the quark-gluon plasma might be too small for the instability to develop.

The origin of this instability of chirally imbalanced Dirac fermions is the chiral magnetic effect (CME) [16,17]—electric current flowing parallel to the magnetic field in the presence of chirality imbalance. Within the linear response approximation the contribution of the CME to the electric current is

$$\vec{j}_{\mathrm{CME}} = \sigma_{\mathrm{CME}} \vec{B}. \tag{1}$$

The commonly quoted value for the chiral magnetic conductivity σ_{CME} is $\sigma_{\mathrm{CME}} = \frac{\mu_A}{2\pi^2}$, where μ_A is the so-called chiral chemical potential, which parametrizes the difference between the Fermi levels of right- and left-handed fermions and hence also the total axial charge of the system. The value of σ_{CME}, however, strongly depends on frequency w and wave vector $\vec{k}$ of the electromagnetic field, and, in the limit of constant and homogeneous magnetic field, on the way in which the limits $w \to 0$ and $k \to 0$ are taken [17–23].

*Pavel.Buividovich@physik.uni-regensburg.de
†Maksim.Ulybyshev@physik.uni-regensburg.de

In order to see how the CME current (1) can lead to instability, one can insert it into the classical Maxwell equations, along with the conventional Ohmic current $\vec{j} = \sigma\vec{E}$, where σ is the electric conductivity. Assuming the unbroken translational invariance both in time and space, we can write these so-called anomalous Maxwell equations [1,3,4,12,13,15,24–26] in frequency-momentum space as

$$iw\vec{B} = -i\vec{k} \times \vec{E}, \qquad iw\vec{E} = i\vec{k} \times \vec{B} - \sigma\vec{E} - \sigma_{\mathrm{CME}}\vec{B}. \tag{2}$$

From these equations we find the following four-branch dispersion relation for transversely polarized plane waves with the wave vector $\vec{k} = k\vec{e}_3$ [15]:

$$w_{s,r} = \frac{i\sigma}{2} + s\sqrt{k^2 + r\sigma_{\mathrm{CME}}k - \frac{\sigma^2}{4}}, \tag{3}$$

where $s = \pm 1$ and $r = \pm 1$ label different branches of the dispersion relation. The corresponding polarization vectors $\epsilon_r = 2^{-1/2}(1, -ir, 0)$ for the electric field $\vec{E}$ correspond to circularly polarized waves with opposite helicities (handedness) for opposite r.

While for nonzero electric conductivity σ the imaginary part of w in (3) is always positive and hence corresponds to decaying plane waves, nonzero chiral magnetic conductivity can also lead to exponentially growing solutions if the absolute value of the wave vector k is smaller than σ_{CME}. From (3) it is also easy to see that for a given wave vector $\vec{k}$, only one of the two helical modes exhibits exponential growth. For example, for $\mu_A > 0$ (and hence $Q_A > 0$ and $\sigma_{\mathrm{CME}} > 0$) and $\sigma_{\mathrm{CME}} > k > 0$ the exponentially growing solution has the form

$$\begin{aligned} &E_1 = fe^{\kappa t}\cos(kx_3), \qquad E_2 = -fe^{\kappa t}\sin(kx_3), \\ &B_1 = -f\frac{k}{\kappa}e^{\kappa t}\cos(kx_3), \qquad B_2 = f\frac{k}{\kappa}e^{\kappa t}\sin(kx_3), \\ &E_3 = 0, \qquad B_3 = 0, \end{aligned} \tag{4}$$

where f is an arbitrary amplitude and $\kappa \equiv -iw = -\frac{\sigma}{2} + \sqrt{\frac{\sigma^2}{4} - k^2 + \sigma_{\mathrm{CME}}k}$. It is important to stress that since this solution grows monotonously in time, here we use the terms "circular polarization," handedness, and helicity to describe the rotation of the vectors $\vec{E}$ and $\vec{B}$ along the x_3 axis, rather than in time. The growth of long-wavelength electromagnetic waves and the decay of short-wavelength waves predicted by the anomalous Maxwell equations (2) is a novel mechanism for the inverse cascade in relativistic magnetohydrodynamics [3,6], which transfers energy from long- to short-wavelength helical magnetic fields.

The fact that the exponentially growing solution (4) has the helical structure of the form (4) also suggests the mechanism that can stop the growth of the electromagnetic field at later times. Namely, let us recall that for massless chiral fermions the time evolution of the axial charge is governed by the anomaly equation,

$$\partial_t Q_A = \frac{g^2}{2\pi^2}\int d^3x\vec{E}\cdot\vec{B}, \tag{5}$$

where the axial charge $Q_A = Q_R - Q_L$ is defined as the difference between the charges Q_R and Q_L of the right- and left-handed fermions, g is the electromagnetic coupling constant, and we have integrated over space to get rid of the spatial divergence of the axial current. For simplicity, in this paper we consider only a single flavor of Dirac fermions with electromagnetic coupling $g = 1$.

For the exponentially growing solution (4) the product $\vec{E}\cdot\vec{B}$ is negative: $\vec{E}\cdot\vec{B} = -f^2\frac{k}{\kappa}e^{2\kappa t}$ [27]. The anomaly equation (5) then dictates that the time derivative $\partial_t Q_A$ of the axial charge is negative. Since we have assumed $Q_A > 0$, $\mu_A > 0$, we see that the growing helical solution (4) results in the decrease of Q_A and hence of μ_A. This depletion of chirality imbalance should eventually suppress the chiral magnetic conductivity in (1) and hence slow down or stop completely the exponential growth in (4).

However, the above analysis of the chiral plasma instability, which follows [3,4,12,13,15,24–26,28], essentially relies on an assumption that the electric current takes the form $\vec{j} = \sigma\vec{E} + \sigma_{\mathrm{CME}}\vec{B}$ with constant Ohmic and chiral magnetic conductivities. In reality, both σ and σ_{CME} depend on the frequency and wave vector of the electromagnetic field in a nontrivial way [17–23]. One can also expect a strong dependence of σ and σ_{CME} on the spatial and temporal modulation of the axial charge density, which in general appears at late evolution times [26]. Moreover, as the instability might lead to quite large strengths of electric and magnetic fields, nonlinear effects beyond the linear response result (1) might become important. Using linear response approximation to describe the interactions between the fermions and the electromagnetic fields is in fact similar to the Lyapunov analysis of the full quantum evolution, which is in general nonlinear. Interfermion interactions so far have been taken into account only indirectly, by using the relaxation time approximation [14] or the decoherence of the fermionic wave functions [29]. A consistent inclusion of all these effects in the anomalous Maxwell equations (2) would certainly be difficult with approaches based, e.g., on the chiral kinetic theory [24–26,30], chiral hydrodynamics [6,31], or the Langevin-type effective theory [32].

This situation clearly calls for a more first-principles description of the real-time dynamics of chirally imbalanced plasma that overcomes these limitations and approximations. In this paper, we report on the numerical study of the real-time chiral plasma instability within the framework of the so-called classical statistical field theory (CSFT) [33–38],

which captures the first nontrivial order of the expansion of the full quantum evolution operator in powers of the Planck constant. CSFT is currently the state-of-the-art method for numerical simulations of real-time quantum evolution. The CSFT approximation is justifiable as long as the characteristic occupation numbers of the physically relevant gauge field modes are large. That is, the dynamics of the gauge fields should be almost classical. On the other hand, the real-time dynamics of fermions is exact in CSFT. Taking into account that in all previous studies gauge fields were also treated classically, the applicability of the CSFT approach is obviously wider than that of the previously used approaches. An approach very similar to CSFT has been recently used in [39] to study the real-time dynamics of the CME. However, in this work the backreaction of fermions on the electromagnetic field, which is the origin of the chiral plasma instability, was not taken into account. The real-time dynamics of axial charge was also studied in the $1+1$-dimensional Abelian Higgs model in the pioneering work of Ref. [33].

Our studies are based on the noncompact formulation of lattice quantum electrodynamics, which avoids potential problems with monopole condensation in the strong-coupling phase [40]. For fermions, we use the massless Wilson-Dirac Hamiltonian, which has a low-energy chiral symmetry. At sufficiently high energies, this symmetry is broken due to the Wilson term. In the condensed matter context, this breaking is a natural feature of any model description of Dirac and Weyl semimetals [41–43]. In Sec. III we demonstrate that the effect of this explicit breaking is, however, not very large (see also [44]). Therefore, we hope that our results are also at least qualitatively relevant in the context of high-energy physics, where the chiral symmetry is exact at the level of the Lagrangian, or tends to be exact at sufficiently high energies.

In order to introduce the initial chirality imbalance, we have started the simulations with a state in which more right-handed eigenstates and less left-handed eigenstates are filled, as depicted on the right panel of Fig. 1. Such a state is an excited state of the many-body Dirac Hamiltonian, even in the absence of electromagnetic fields. It is an idealized description of the result of the chirality pumping process in parallel electric and magnetic fields [9,45] or in intense circularly polarized laser beams.

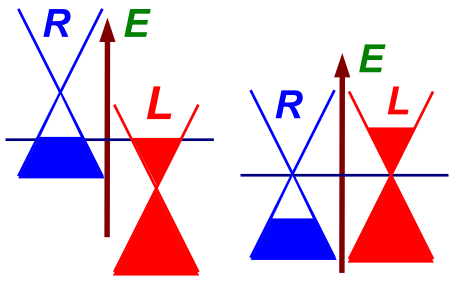

FIG. 1. Two ways of introducing initial chiral imbalance for the many-body Dirac Hamiltonian: on the left, by introducing the chiral chemical potential μ_A in the single-particle Dirac Hamiltonian; and on the right, by filling more right-handed eigenstates and less left-handed eigenstates (or vice versa).

Alternatively, we have also considered the introduction of the chiral chemical potential into the single-particle Dirac Hamiltonian, which changes the energies of the right- and the left-handed Dirac points (see the left panel of Fig. 1). Such an initial state has nonzero axial charge but is still the ground state of the many-body Hamiltonian in the absence of interactions with electromagnetic fields. In simulations that started from this state we have not found any signatures of instability or the transfer of helicity from fermions to electromagnetic fields. The axial charge density exhibited only small fluctuations on top of the large mean value. Presumably, the reason for such a behavior is that nonzero chiral chemical potential corresponds to the physical situation in which our system is connected to an infinite reservoir of axial charge, which is capable of maintaining its initial value at a constant level. Since the anomaly equation (5) holds also at nonzero chiral chemical potential, this also implies that the magnetic helicity can only exhibit small fluctuations, possibly related to the violation of the anomaly equation due to lattice artifacts. Since such behavior is not really interesting, we do not discuss this setup in what follows.

The structure of this paper is the following: in Sec. II we start with a brief summary of the details of our numerical CSFT algorithm. In Appendix A we provide a more detailed derivation of this algorithm with a bias towards non-relativistic field theories and condensed matter systems, which will hopefully complement the existing literature on CSFT (see, e.g., [33,38] for derivations that are more in the spirit of relativistic quantum field theory). In this appendix we also demonstrate explicitly the absence of any nontrivial Jacobian in the integration measure in the CSFT algorithm, and discuss some practical aspects of our CSFT simulations on parallel computers. In Sec. III we present the results of the simulations of the chirality pumping process. First, we consider chirality pumping in external parallel electric and magnetic fields in the absence of backreaction and verify the validity of the anomaly equation (5) in our numerical setup. After that we consider the effect of backreaction of fermionic current on the chirality pumping process and demonstrate that the dynamical screening of the external electric field prevents the system from acquiring large axial charge density at late evolution times.

In Sec. IV, we consider the decay of the initial chiral imbalance and the generation of electromagnetic fields with nonzero helicity. In order to trigger the decay, we start simulations with several initially excited modes of electromagnetic field. Following the energies of helical modes in momentum space, we demonstrate that only long-wavelength modes of definite helicity grow and all other modes decay with time. This is direct numerical evidence of the

inverse cascade phenomenon [3,6,12,46] due to chiral plasma instability. We find, however, that the dependence of the strength of the inverse cascade on the initial conditions and parameters of the simulations is significantly more complex than predicted by the anomalous Maxwell equations (2). In particular, in the simulations that exhibit the most rapid growth of helical magnetic fields the axial charge does not decay at all. Correspondingly, the mechanism that stops the inverse cascade in our simulations is not related to the axial charge decay, again in contrast to the expectations based on Eqs. (2) [3,4,6,12–14]. Rather, we observe that in most simulations that do exhibit axial charge decay the inverse cascade emerges for the electric rather than for magnetic fields. In Sec. V we conclude with a general discussion of our results and an outlook.

II. CLASSICAL STATISTICAL FIELD THEORY APPROXIMATION TO REAL-TIME EVOLUTION

We consider the many-body fermionic Hamiltonian coupled to dynamical noncompact electromagnetic fields on the lattice, so that the full Hamiltonian $\hat{H}$ of our system is $\hat{H} = \hat{H}_F + \hat{H}_{\mathrm{EM}}$. The fermionic Hamiltonian $\hat{H}_F$ reads

$$\hat{H}_F = \sum_{x,y} \hat{\psi}_x^\dagger h_{x,y} \hat{\psi}_y, \tag{6}$$

where the labels x, y denote the sites of the three-dimensional cubic lattice, $\hat{\psi}_x^\dagger, \hat{\psi}_x$ are the spinor-valued fermionic creation and annihilation operators that satisfy the anticommutation relation $\{\hat{\psi}_x^\dagger, \hat{\psi}_y\} = \delta_{xy}$, and $h_{x,y}$ is the massless single-particle Wilson-Dirac Hamiltonian with the Wilson coefficient $r = 1$,

$$h_{x,y} = 3v_F \beta \delta_{x,y} + \frac{iv_F}{2} \sum_{i=1}^{3} (i\beta + \alpha_i) e^{igA_{x,i}} \delta_{y,x+e_i} + \frac{iv_F}{2} \sum_{i=1}^{3} (i\beta - \alpha_i) e^{-igA_{x-e_i,i}} \delta_{y,x-e_i}. \tag{7}$$

Here $A_{x,i}$ is the vector potential of the lattice gauge field, e_i denotes the unit lattice vector in the direction i, v_F is the Fermi velocity, β and α_i are the Dirac β and α-matrices, and γ_5 is the generator of chiral rotations,

$$\beta = \begin{pmatrix} 0 & 1 \\ 1 & 0 \end{pmatrix}, \qquad \alpha_i = \begin{pmatrix} \sigma_i & 0 \\ 0 & -\sigma_i \end{pmatrix}, \qquad \gamma_5 = \begin{pmatrix} 1 & 0 \\ 0 & -1 \end{pmatrix}, \tag{8}$$

where σ_i are the Pauli matrices. In (7) we have assumed that the lattice spacing is unity. Thus, in what follows all dimensionful quantities are expressed in units of the lattice spacing.

The lattice Hamiltonian $\hat{H}_{\mathrm{EM}}$ of the electromagnetic field is the straightforward lattice discretization of the corresponding continuum Hamiltonian,

$$\hat{H}_{\mathrm{EM}} = \sum_x \sum_{i=1}^{3} \left(\frac{\hat{E}_{x,i}^2}{2} + \sum_{j=i}^{3} \frac{\hat{F}_{x,ij}^2}{2} + \hat{A}_{x,i} \mathcal{J}_{x,i}(t) \right), \tag{9}$$

where $\mathcal{J}_{x,i}(t)$ is the external current (which is required, e.g., to switch the external electric and magnetic fields on and off) and the operator of the magnetic field strength tensor $\hat{F}_{x,ij}$ is defined in terms of the finite differences of the vector potential operator $\hat{A}_{x,i}$ as

$$\hat{F}_{x,ij} = \hat{A}_{x,i} + \hat{A}_{x+e_i,j} - \hat{A}_{x+e_j,i} - \hat{A}_{x,j}. \tag{10}$$

The operators of the electric field $\hat{E}_{x,i}$ and the vector potential $\hat{A}_{x,i}$ are canonically conjugate and satisfy the commutation relations $[\hat{E}_{x,i}, \hat{A}_{y,j}] = -i\delta_{xy}\delta_{ij}$. We impose periodic boundary conditions in all spatial directions both for the gauge and the fermionic fields.

In our CSFT algorithm, described in detail in Appendix A, we numerically solve the classical equations of motion of the electromagnetic field with the Hamiltonian (9),

$$\partial_t^2 A_{x,i}(t) = -\mathcal{J}_{x,i}(t) - \langle j_{x,i}(t) \rangle - \sum_j (F_{x,ij}(t) - F_{x-e_j,ij}(t)), \tag{11}$$

where the initial value of the time derivative $\partial_t A_{x,i}(t)|_{t=0}$ is the initial value of the electric field $E_{x,i}(0)$ and $\langle j_{x,i}(t) \rangle$ is the vacuum expectation value of the fermionic electric current, which can be calculated as

$$\langle j_{x,i}(t) \rangle = \mathrm{Tr}(\rho_0 u(0,t) j_{x,i} u^\dagger(0,t)), \tag{12}$$

where $j_{x,i} = \frac{\partial h}{\partial A_{x,i}}$ is the single-particle operator of electric current, $u(0,t)$ is the quantum evolution operator defined by the single-particle Schrödinger equation

$$\partial_t u(0,t) = ih[A_{x,i}(t)] u(0,t), \qquad u(0,0) = I, \tag{13}$$

and ρ_0 is the initial density matrix that characterizes the initial occupation numbers n_a of single-particle states $|\psi_a\rangle$,

$$\rho_0 = \sum_a |\psi_a\rangle n_a \langle \psi_a|. \tag{14}$$

In our case, $|\psi_a\rangle$ are the eigenstates of the single-particle Hamiltonian (7). If some occupation numbers are exactly 0 (which can be the case at zero temperature), some components of the quantum evolution operator u completely

decouple and can be discarded in the solution of the equation (13). This can be used to speed up the algorithm, typically by a factor of 2 (for a standard zero-temperature Fermi distribution). The expectation value $\langle j_{x,i}(t)\rangle$ in (11) describes the effect of backreaction of fermions on the electromagnetic fields.

We thus have a closed set of equations (11)–(13), which allows us to evolve the fermionic quantum states and the classical electromagnetic fields in a self-consistent way. One can also explicitly check that this evolution conserves the total energy $H_{\rm EM} + \langle \hat{H}_F \rangle$ of the electromagnetic field and fermions up to the work done by the external current $\mathcal{J}^{x,i}(t)$,

$$\begin{aligned} \partial_t (H_{\rm EM} + \langle \hat{H}_F \rangle) &= -\sum_{x,i} \mathcal{J}_{x,i}(t) E_{x,i}(t), \\ H_{\rm EM} &= \frac{1}{2} \sum_{x,i} \left((\partial_t A_{x,i})^2 + \sum_j F_{x,ij}^2 \right), \\ \langle \hat{H}_F \rangle &= {\rm Tr}(\rho_0 u(0,t) h u^\dagger(0,t)). \end{aligned} \tag{15}$$

We have solved the evolution equations (11) and (13) using the leapfrog integrator, which slightly violates the conservation of energy (15). At a sufficiently small time step this violation is completely under numerical control; see Fig. 14 in Appendix A.

In the CSFT approach, one can also partially take into account the quantum fluctuations of the electromagnetic fields, encoded in the nontrivial Wigner transform $\bar{\rho}_{\rm EM}(A_0, E_0)$ of the initial density matrix $\rho_{\rm EM}$, where $A_0 \equiv A(t=0)$ and $E_0 \equiv E(t=0)$ are the initial values of electric and magnetic fields. To this end one should additionally average all observables over A_0 and E_0, sampled with the probability $\bar{\rho}_{\rm EM}(A_0, E_0)$ [47]. However, in our work we have not taken these initial quantum fluctuations into account for the following reasons. First, in the case of anomaly equation (5) with massless fermions we have found that the effect of initial fluctuations of electromagnetic fields is much more significant than in the case of, e.g., Schwinger pair production [38] [48], and hence many more samples of the initial fields are required to reach acceptable statistical errors. Partially this can be explained by the large value of the electromagnetic coupling constant, which was $g = 1.0$ in most of our simulations. We expect that the role of initial fluctuations will be smaller for a smaller value of g, say $g = 0.1$. In the latter case, however, the characteristic time scale of the chiral plasma instability increases significantly above our current simulation times.

In addition, taking into account initial quantum fluctuations of electromagnetic fields makes it impossible to assume spatial homogeneity of electromagnetic fields along some of the lattice directions, which is essential to speed up the CSFT simulations at large lattice sizes.

Thus, while the effect of quantum fluctuations on the chiral plasma instability might be potentially very significant and interesting, we cannot study it with our presently available computational resources and we leave it for future work. In this work, we avoid the statistical averaging over the initial values of the fields E_0, A_0 by using the very simple form of the initial density matrix $\bar{\rho}_{\rm EM}(A_0, E_0)$, which is just a delta function on some particular, specifically chosen initial values. We thus completely neglect the quantum fluctuations of the electromagnetic fields. Nevertheless, this approximation is still certainly wider than the chiral kinetic theory or hydrodynamical approximation.

III. CHIRALITY PUMPING IN PARALLEL ELECTRIC AND MAGNETIC FIELDS

In this section we study the real-time evolution of the axial charge Q_A in the background of constant parallel external electric and magnetic fields. In the absence of backreaction, such a setup provides a direct check of how well the anomaly equation (5) holds for the Wilson-Dirac Hamiltonian with inexact chiral symmetry [44], which we further use to study the chiral plasma instability in Sec. IV. The effect of backreaction is also interesting since the anomaly equation (5) is known to receive nontrivial corrections if the electromagnetic fields are dynamical [49–51].

In order to induce the constant external electric field $\vec{E} = E\vec{e}_3$, we switch on the external current of the form $\mathcal{J}_{x,i}(t) = \delta_{i,3} E t$. Constant external magnetic field is induced by the static circular external current flowing around the plaquettes with $x_1 = L_1 - 1$, $x_2 = L_2 - 1$ for all $x_3 = 0 \ldots L_3 - 1$, where L_1, L_2 and L_3 are lattice sizes. This static current is like a thin solenoid piercing a stack of lattice plaquettes, with the field strength being equal to B outside of the solenoid and $B - BL_1L_2$ inside it. Lattice fermions, however, acquire only the Aharonov-Bohm phase e^{igB} when encircling such a solenoid if one imposes the flux quantization condition

$$gBL_1L_2 = 2\pi\Phi, \qquad \Phi \in \mathbb{Z}. \tag{16}$$

The total external current that we insert in Eqs. (11) is the sum of the two currents that create constant electric and magnetic fields.

For the initial state of the fermionic fields, we use the eigenstates of the Wilson-Dirac Hamiltonian $h[A_0]$, where A_0 is the initial gauge field configuration with constant magnetic field B as described above. In this work we consider only the limit of zero temperature; correspondingly, only the states with negative energies are initially occupied.

The Wilson-Dirac Hamiltonian that we use in our simulations does not have exact chiral symmetry, and there is no uniquely defined axial charge operator that would

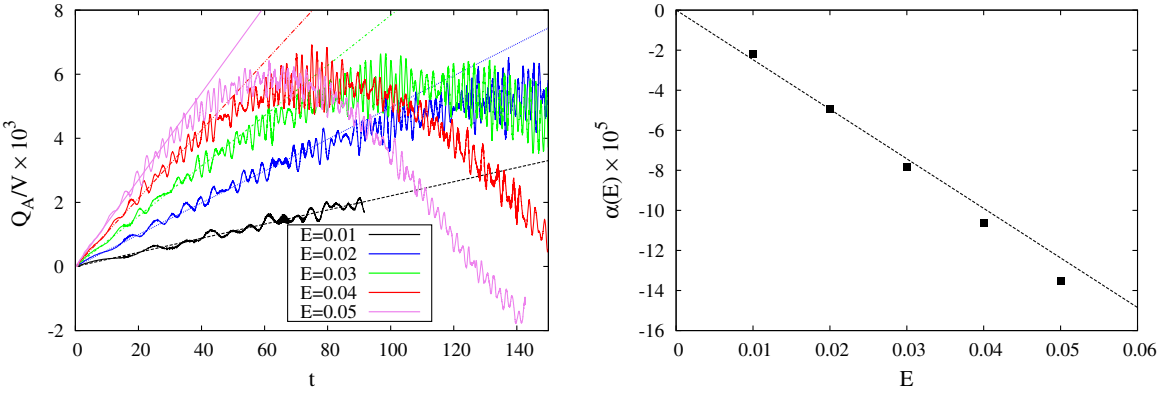

FIG. 2. Chirality pumping without backreaction for various external electric fields and external magnetic field with flux $\Phi = 1$ on the $10 \times 10 \times 32$ lattice. On the left is the time dependence of the axial charge Q_A and its linear fits at early times. On the right is dependence of the slope of these fits on the external electric field and the linear fit of this dependence. Here and in what follows time is expressed in units of lattice spacing.

exactly satisfy the anomaly equation (5) and commute with the Hamiltonian. Rather, the anomaly equation (5) can only hold approximately, in the limit of large lattice volume and sufficiently smooth, slowly changing and small gauge fields [52,53]. We thus use the simplest possible definitions of the operators of the axial charge density q_{Ax} and the total axial charge Q_A,

$$\hat{q}_{Ax} = \hat{\psi}_x^\dagger \gamma_5 \hat{\psi}_x, \qquad \hat{Q}_A = \sum_x \hat{q}_{Ax}. \tag{17}$$

The time-dependent expectation value of the axial charge density is calculated similarly to the expectation value of the electric current in (12),

$$\langle q_{Ax}(t) \rangle = \mathrm{Tr}(\rho_0 u(0,t) \gamma_5 P_x u^\dagger(0,t)), \tag{18}$$

where P_x is the single-particle projector on a single lattice site x: $[P_x]_{x_1 x_2} = \delta_{x_1 x} \delta_{x x_2}$.

First, we neglect the backreaction of the fermionic electric current on the electromagnetic field and measure the time dependence of the axial charge in constant parallel external electric and magnetic fields. The results are shown on the left panel of Fig. 2 for the $10 \times 10 \times 32$ lattice with $\Phi = 1$ quantum of magnetic field flux. One can see that Q_A grows linearly with time until it reaches some maximal value $Q_A/V \approx 0.006$, where $V = L_1 L_2 L_3$ is the total number of lattice sites (lattice volume). After that, Q_A decreases again. This decrease is a lattice artifact related to the fact that the characteristic momentum $p \sim Et$ of fermions accelerated by an electric field E approaches the UV cutoff set by the compact size of the lattice momentum space $k_\mu \in [-\pi \ldots \pi]$. Because of the periodicity of lattice momentum space, at large time scales the behavior of the axial charge (in the absence of backreaction) is well described by $Q_A \sim \sin(Et/2)$. There are also some short-time fluctuations on top of the clearly visible linear growth at early times.

In order to estimate the linear growth rate at early times, we perform the linear fit of the form $Q_A(t)/V = \alpha(E)t$ in the range $t \in [0 \ldots 50]$ for $E = 0.01$ and $E = 0.02$ and in the range $t \in [0 \ldots 30]$ for other values of E. The dependence of the coefficient $\alpha(E)$ on the electric field is shown on the right panel of Fig. 2. Again, this dependence is linear with a good precision, and we perform another linear fit $\alpha(E) = CE$, where C corresponds to the anomaly coefficient relating $\partial_t Q_A$ and $\int d^3\vec{x}\, \vec{E} \cdot \vec{B}$ in (5). On Fig. 3 we show the dependence of C on the size of the lattice (in the directions perpendicular to the magnetic field). One can see how C approaches the value $C = \frac{1}{2\pi^2}$ in the limit of large lattices, in agreement with the anomaly equation (5). Let us also note that for a larger number of flux quanta one can perform a similar fitting procedure. However, finite-volume artifacts in C are significantly larger for larger magnetic fluxes. For this reason, in this work we have only used external magnetic fields with one flux quantum.

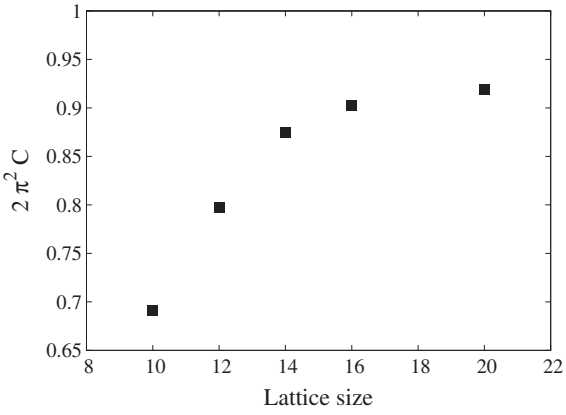

FIG. 3. Dependence of the lattice anomaly coefficient ($\partial_t Q_A = C \int d^3\vec{x}\, \vec{E} \cdot \vec{B}$) on the transverse lattice size. Lattice size in the direction parallel to the magnetic field is fixed to $L_3 = 32$.

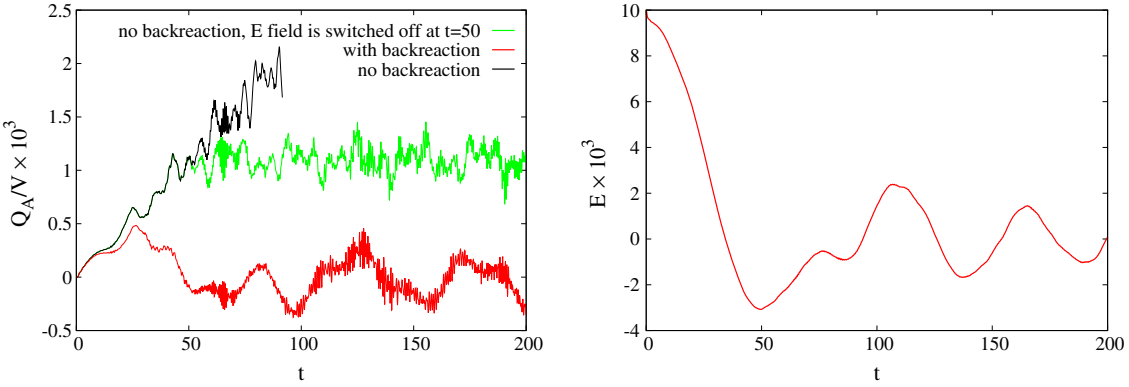

FIG. 4. A comparison of chirality pumping processes with and without backreaction of the fermionic electric current on the electromagnetic field. On the left is time dependence of the axial charge. On the right is time dependence of the component of the volume-averaged electric field parallel to the magnetic field. Lattice size is $10 \times 10 \times 32$, the flux of the external magnetic field is $\Phi = 1$, and external electric field is 0.01.

It is also interesting to check how the axial charge depends on time after the external electric field is switched off and the external magnetic field remains constant (which we believe to be a more realistic experimental setup than the simultaneous switching off of all fields). The time dependence of the axial charge for such a situation is shown on the left plot of Fig. 4 (green line). External electric field is switched off at the time $t = 50$. One can see that starting from this moment of time the axial charge exhibits only some small-scale fluctuations around the nonzero mean value. This demonstrates that the effect of explicit chiral symmetry breaking due to the Wilson term in the Hamiltonian (7) is rather small for such simulation parameters, and the total axial charge is almost a conserved quantity.

After establishing the validity of the anomaly equation (5) in our simulation setup, we study the effect of backreaction of dynamical electromagnetic fields on the chirality pumping process. Technically, the backreaction is taken into account by inserting the expectation value of the fermionic electric current $\langle j_{x,i} \rangle$ into the Maxwell equations for the electromagnetic field. We now consider the situation in which the external electric and magnetic fields are switched on permanently. As we will see, in simulations with backreaction switching off the electric field at sufficiently late times anyway does not affect the evolution significantly due to screening by the dynamically generated electric field. Time dependence of the axial charge $Q_A(t)$ for the simulation with backreaction is shown on Fig. 4. For comparison, in the same figure we also show $Q_A(t)$ for simulations without backreaction, where the electric field is permanent or switched off at $t = 50$.

One can see that while at $t \lesssim 30 Q_A(t)$ grows approximately linearly with t both with and without backreaction, at later times backreaction leads to a rapid decay of Q_A with subsequent fluctuations around 0. In order to understand the origin of this effect, remember that axial anomaly can also be regarded as the Schwinger pair production in the effective $1+1$-dimensional theory of fermions on the lowest Landau level. It is thus natural to expect that particle-antiparticle pairs produced by the external electric field will tend to screen this field, just as in the case of the Schwinger effect in $(3+1)$ dimensions. To check this conjecture, on the right panel of Fig. 4 we plot the volume-averaged electric field projected in the direction of the magnetic field. One can see that indeed it quite quickly decreases from the initial value $E = 0.01$, reaching 0 at around $t \approx 30$, exactly at the time at which the growth of the axial charge stops (see the left panel of the same figure). After that the electric field exhibits some fluctuations around 0 with the amplitude, which is approximately five times smaller than the initial field value. We thus conclude that the effect of backreaction on the chirality pumping is to stop the growth of the axial charge by screening the external electric field down to 0.

IV. CHIRAL PLASMA INSTABILITY AND DECAY OF AXIAL CHARGE

In this section, we consider a situation in which some initial chiral imbalance is already created, e.g., by chirality pumping, and the parallel electric and magnetic fields are adiabatically switched off while keeping nonzero the value of the total axial charge Q_A and hence the chiral chemical potential μ_A. In this setup we study the existence and the late-time evolution of the exponentially growing solutions (4) of the anomalous Maxwell equations (2), as well as the associated inverse cascade of energy of helical electromagnetic fields.

In order to implement the initial chirality imbalance as discussed in Sec. I (see the right panel of Fig. 1), we divide all the eigenstates of the single-particle Wilson-Dirac Hamiltonian $h[A_0]$, where A_0 is the initial value of the vector potential, into the positive chirality states with $\langle \psi_a | \gamma_5 | \psi_a \rangle > 0$ and the negative chirality states with $\langle \psi_a | \gamma_5 | \psi_a \rangle < 0$. For positive chirality states we fill all

the levels with $\epsilon_a < \mu_A$, and for negative chirality states we fill all the levels with $\epsilon_a < -\mu_A$. While the eigenstates of the Wilson-Dirac Hamiltonian are not in general the eigenstates of the γ_5 operator, for eigenstates with sufficiently small momenta our definition is maximally close to the notion of distinct Fermi levels of left- and right-handed continuum massless fermions. In practice, this definition is unambiguous as long as all the energy levels ϵ_a are nondegenerate. In the case of degenerate energy levels (as, e.g., in the case of the Wilson-Dirac Hamiltonian with zero gauge fields or in the background of a single plane wave), one can additionally rotate the eigenstates within the degenerate subspaces in order to maximize the absolute values of matrix elements $\langle\psi_a|\gamma_5|\psi_a\rangle$.

With lattice discretizations of the Dirac Hamiltonian it is not possible to have very large values of the chiral chemical potential μ_A, since the dispersion relation at the Fermi energy $\mu_A \gtrsim 1$ starts deviating from the Dirac cone $\epsilon(\vec{k}) = v_F|\vec{k}|$ due to lattice artifacts. At $\mu_A = 2$, the Fermi energy touches the lowest van Hove singularity (saddle point) of the dispersion relation, and the excitations around the Fermi surface no longer correspond to Dirac fermions. On the other hand, the solution (4) of the anomalous Maxwell equations (2) with the conventional value $\sigma_{\mathrm{CME}} = \frac{\mu_A}{2\pi^2}$ of the chiral magnetic conductivity suggests that the wave vectors at which the chiral plasma instability can occur are bounded by $|\vec{k}| < \frac{\mu_A}{2\pi^2}$. On a finite spatial lattice of size L with periodic boundary conditions, the smallest nonzero value of $|\vec{k}|$ is $|\vec{k}| = \frac{2\pi}{L}$, which dictates the lower bound on the size of the lattice where the instability can be observed,

$$L > \frac{4\pi^3}{\mu_A}. \tag{19}$$

Thus, it is advantageous to use large values of μ_A in order to reduce the lattice size used for simulations. Taking the moderate value $\mu_A = 0.75$, at which the dispersion relation is still linear with a good precision, we obtain $L > 165$. Performing simulations on an isotropic three-dimensional lattice of such a size is a formidable numerical task. For this reason we have used the lattices with different sizes in different directions, so that the size L_3 in the direction x_3 of electromagnetic wave propagation is much larger than the sizes $L_1 = L_2 \equiv L_s$ in the transverse directions x_1 and x_2. In addition, we have assumed that electromagnetic fields do not depend on the transverse coordinates x_1 and x_2. This allows us to represent the single-particle evolution operator $u(0, t)$ in the block-diagonal form in the basis of plane waves propagating along x_1 and x_2, which greatly reduces the dimensionality of the linear space on which the single-particle Schrödinger equation (13) should be solved. By comparing the results of simulations with $L_s = 20$ and $L_s = 40$ at fixed $L_3 = 200$ (see Table I and Figs. 5, 6, 10, 11, and 12) we have checked that the dependence on the transverse lattice size is rather weak. Let us also note that one of the reasons for not using the final state of the chirality pumping process described in Sec. III for the study of chiral plasma instability is that in this case it is not possible to assume spatial homogeneity in transverse directions due to the breaking of translational invariance by the external magnetic field [54].

TABLE I. Summary of parameters and results of our simulations of chiral plasma instability. The column $Q_A\downarrow$ summarizes the decay of the axial charge and the columns $I_k^{E,B}\uparrow$ summarize the growth of the energies of long-wavelength electric and magnetic fields. The symbols ✓, ×, and **?** denote, respectively, the clearly visible growth, clearly visible absence of growth, and intermediate situations for which it is difficult to make any conclusion within a finite simulation time.

Set No.	L_3	L_s	μ_A	n	f	v_F	$Q_A\downarrow$	$I_k^B\uparrow$	$I_k^E\uparrow$
1	200	20	0.75	10	0.20	1.00	✓	×	✓
2	200	40	0.75	10	0.20	1.00	✓	×	✓
3	200	20	1.50	10	0.20	1.00	✓	✓	✓
4	200	20	0.75	10	0.05	1.00	×	✓	×
5	200	20	0.75	4	0.20	1.00	✓	✓	?
6	200	20	0.75	4	0.05	1.00	×	✓	?
7	200	20	1.50	10	0.05	1.00	×	✓	?
8	200	20	0.75	10	0.20	0.75	✓	×	✓
9	20	20	1.00	1	0.20	1.00	✓	×	×

While the fermionic initial state described above is an excited state that can spontaneously decay due to chiral plasma instability, in numerical simulations one always needs some small seed perturbation to start the decay process in a controllable way. For this reason we have started our simulations with a state in which some finite number n of electromagnetic field modes are also excited. All of them are plane waves propagating along the lattice direction x_3 with the largest size L_3, with a few of the smallest nonzero wave numbers $k_m = \frac{2\pi m}{L_3}$, $m = 1 \ldots n$ and random linear polarizations. In order to facilitate the detection of the inverse cascade, we choose the amplitudes of all modes in such a way that their contributions to the total energy of electromagnetic field are equal. Thus, the explicit form of our initial electromagnetic field configuration is

$$\begin{aligned} A_{x,i}(t=0) &= \sum_{m=1}^{n} \frac{f}{w(k_m)} n_{mi} \cos(k_m x_3 + \phi_m), \\ E_{x,i}(t=0) &\equiv \partial_t A_{x,i}(t)|_{t=0} \\ &= \sum_{m=1}^{n} f n_{mi} \sin(k_m x_3 + \phi_m), \end{aligned} \tag{20}$$

where n_{mi} are the random unit transverse polarization vectors that are chosen to coincide with one of the basis vectors $\vec{e}_1$, $\vec{e}_2$ with equal probability, $\phi_m \in [0, 2\pi]$ are the random phases, and $w(k_m) = \sqrt{4\sin^2(\frac{k_m}{2})}$ corresponds to

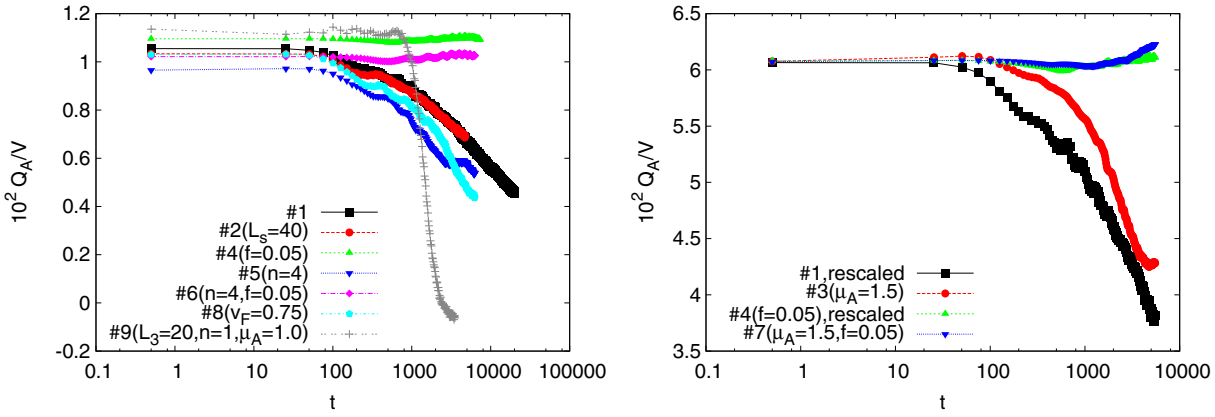

FIG. 5. Time dependence of the total axial charge for different simulation parameters. On the right plot we compare simulations with different μ_A and linearly rescale $q_A(t) \to cq_A(t)$ so that the initial values of $cq_A(0)$ agree for all simulations. In the plot labels, numbers preceded by the hash symbol # correspond to the numbers of parameter sets in Table I. In parentheses we give the values of only those parameters that differ from the default parameters ($L_3 = 200$, $L_s = 20$, $\mu_A = 0.75$, $n = 10$, $f = 0.2$, and $v_F = 1$, parameter set number 1).

the lattice dispersion relation for free massless fields on the lattice.

In order to understand how the evolution process depends on various lattice parameters, we have performed simulations with nine different parameter sets, which are summarized in Table I. We have varied both the transverse and the longitudinal lattice sizes, the initial electromagnetic field amplitude f, the number n of initially excited electromagnetic field modes, the initial value of the axial charge, and the Fermi velocity v_F. The parameter set number 1 with $L_3 = 200$, $L_s = 20$, $\mu_A = 0.75$, $n = 10$, $f = 0.2$, and $v_F = 1$ is the "default" parameter set, and all other sets differ from it by a change in a few parameters. Correspondingly, in what follows we label the data points on the plots that combine the results from several simulations by the number of parameter sets (preceded by the hash symbol #), in parentheses giving only those parameters that differ from the default ones.

In Fig. 5 we show the time dependence of axial charge in simulations with parameters summarized in Table I. In simulations with the initial amplitude of electromagnetic fields being equal to $f = 0.2$ the axial charge Q_A decays with time. Interestingly, simulations with the smallest lattice size (parameter set number 9) exhibit the fastest decay of Q_A. On the other hand, with the initial amplitude $f = 0.05$ the axial charge density exhibits only a rather small decrease at intermediate evolution times, subsequently followed by a slight increase. This nontrivial dependence on the electromagnetic field strength suggests that the dynamics of the decay process is more complicated than suggested by the anomalous Maxwell equations (2). It is interesting that the evolution of the axial charge seems to depend only weakly on simulation parameters other than the initial amplitude f and the longitudinal lattice size L_3 (through the value of the lowest wave number $\frac{2\pi}{L_3}$). Even the dependence on the chiral chemical potential μ_A appears to be rather weak (after a trivial rescaling with respect to the initial value); see the right plot in Fig. 5. The characteristic time scale for the evolution of the axial charge appears to be essentially larger than in the chirality pumping simulations in the previous section. This difference can be qualitatively explained by much weaker field strengths in the simulations described in this section. We also note that the initial values of the axial charge are roughly consistent with the continuum formula $Q_A/V = \mu_A^3/(3\pi^2)$, where V is the lattice volume. Deviations from this value can be explained, first, by the inclusion of the initial vector potential A_0 in the initial Hamiltonian, and second, by the smaller value of chirality $|\langle\psi_a|\gamma_5|\psi_a\rangle| < 1$ for high-energy eigenstates $|\psi_a\rangle$ of the Wilson-Dirac Hamiltonian (7).

A scaling analysis of the anomalous Maxwell equations suggests that at late evolution times the time dependence of

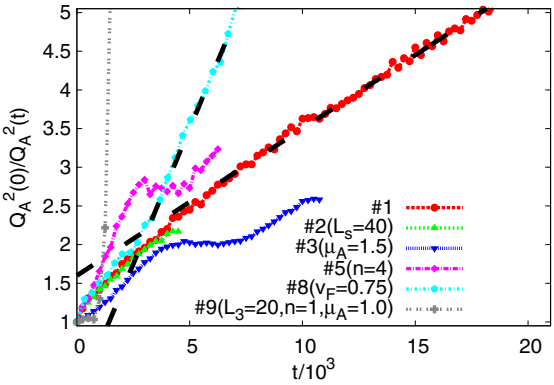

FIG. 6. Universal late-time scaling $Q_A(t) \sim 1/\sqrt{t}$ of axial charge density in simulations with $f = 0.2$. Time dependence of $(Q_A(0)/Q_A(t))^2$ in the second half of the total evolution time is fitted, where appropriate, by linear functions $(Q_A(0)/Q_A(t))^2 = A + Bt$. The fits are shown with dashed black lines.

the axial charge density approaches the simple power law [12,46],

$$Q_A(t) \sim 1/\sqrt{t}. \tag{21}$$

In order to check this scaling, in Fig. 6 we plot the time dependence of the inverse square of the axial charge, which should approach the linear function $1/Q_A^2(t) \sim t$ according to (21). This asymptotic behavior indeed seems to emerge at late evolution times for simulations with $L_s = 20$, $n = 10$, $f = 0.2$, and $\mu_A = 0.75$, both with $v_F = 1$ and $v_F = 0.75$ (parameter sets number 1 and 8). The linear fits of $(Q_A(0)/Q_A(t))^2$ for these simulations are shown in Fig. 6 with dashed black lines.

We now check whether the decay of the axial charge is accompanied by the growth of the long-wavelength modes of the electromagnetic field, as predicted by the anomalous Maxwell equations (2). To this end we perform the Fourier transforms of the transverse electric and magnetic fields (taking into account that they depend only on the x_3 coordinate),

$$E_{k,i}(t) = \frac{1}{\sqrt{L_3}} \sum_{x_3} e^{ikx_3} E_{x,i}(t),$$
$$B_{k,i}(t) = \frac{1}{\sqrt{L_3}} \sum_{x_3} e^{ikx_3} B_{x,i}(t), \tag{22}$$

where $i = 1, 2$, and further decompose the Fourier-transformed fields into the helical components $E_{k,R/L}(t)$ and $B_{k,R/L}$ with right- and left-handed helicities,

$$B_{k,R}(t) = \frac{1}{2}(B_{k,1}(t) + B_{-k,1}(t)) + \frac{1}{2i}(B_{k,2}(t) - B_{-k,2}(t)),$$
$$B_{k,L}(t) = \frac{1}{2i}(B_{k,1}(t) - B_{-k,1}(t)) + \frac{1}{2}(B_{k,2}(t) + B_{-k,2}(t)). \tag{23}$$

For electric fields, the definition of helical components is exactly the same. Again, here the term helicity refers to the direction of rotation of transverse electric and magnetic fields along the spatial direction of wave propagation (the x_3 axis in our setup).

After such a decomposition, we calculate the energies of left- and right-handed helical electric and magnetic fields with a given wave number k as

$$I^B_{k,R/L}(t) = |B_{k,R/L}(t)|^2/2 + |B_{-k,R/L}(t)|^2/2,$$
$$I^E_{k,R/L}(t) = |E_{k,R/L}(t)|^2/2 + |E_{-k,R/L}(t)|^2/2, \tag{24}$$

where $k = \frac{2\pi m}{L_3}$ and $m = 0 \ldots \lfloor L_3/2 \rfloor$ now spans only half of the discrete lattice momenta. Since the initial configuration of electromagnetic fields contains plane waves with (random) linear polarizations and equal energies, at $t = 0$ the energies $I_{k,R/L}(t)$ of all left- and right-handed electromagnetic modes with $0 < k \leq \frac{2\pi n}{L_3}$ are equal.

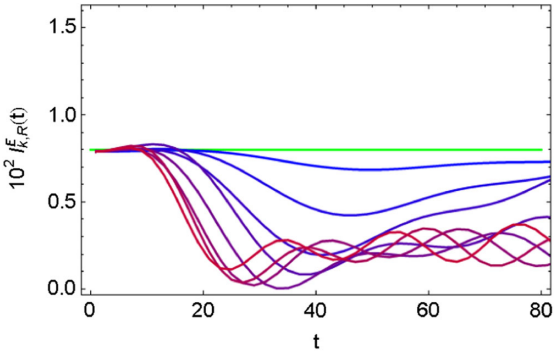

FIG. 7. Time dependence of the energies $I^E_{k,R/L}(t)$ of right-handed components of the electric field on a short time interval at the beginning of the evolution for parameter set number 1 ($L_s = 200$, $n = 10$, $\mu_A = 0.75$, $f = 0.2$). The wave numbers are coded in color, from pure blue for the smallest nonzero value $k = \frac{2\pi}{L_3}$ (largest wavelength) to pure red for $k = \frac{2\pi n}{L_3}$.

We have found that for all simulations the energies $I^{E,B}_{k,R/L}(t)$ exhibit quite large short-scale fluctuations with a period of order $\Delta t \sim 10 \ldots 100$, which is smaller for short-wavelength modes and larger for long-wavelength ones. For illustration, see Fig. 7, where we plot the time dependence of $I^E_{k,R}(t)$ within a short initial period of time for simulation with parameter set number 1. These oscillations indicate that the helical magnetic and electric fields represented by the basis (23) are not the eigenstates of the evolution process, which is in sharp contrast to the solution (4) of the anomalous Maxwell equations (2). We have explicitly checked that if the backreaction of fermions on the electromagnetic fields is neglected, these oscillations disappear and the energies $I^{E,B}_{k,R/L}(t)$ are constant in time for all values of k and for all polarizations. This observation suggests that the short-scale oscillations might originate from the nontrivial dependence of fermionic current on the frequency, wave number, and amplitude of the electromagnetic field, which turns the solutions of the anomalous Maxwell equations (2) into waves with generic elliptic polarizations.

Despite the short-scale fluctuations, we still find it useful to decompose our fields in the basis (23), since the corresponding electromagnetic modes carry definite helicity and thus the energies of helical modes can be used to define, at least approximately, the helicity on the lattice. This definition is advantageous since direct lattice discretizations of the continuum formula $\mathcal{H} \sim \int d^3x \vec{A} \cdot \vec{B}$ are in general flawed by lattice artifacts. In order to abstract ourselves from the short-scale fluctuations, we define the energies $\bar{I}_{k,R/L}(t)$ that are averaged over some finite time interval T,

$$\bar{I}^{E,B}_{k,R/L}(t) = \frac{1}{T}\int_{t-T/2}^{t+T/2} dt' I^{E,B}_{k,R/L}(t'). \tag{25}$$

We have used the value $T = 25$, which is sufficient to remove practically all short-scale oscillations.

In Figs. 8 and 9 we separately illustrate the time dependence of the energies of the left-handed (on the left) and right-handed (on the right) helical magnetic and electric fields with wave numbers $k \le \frac{2\pi n}{L_3}$ for several of the most characteristic sets of simulation parameters. The wave numbers are coded in color, from pure blue for the smallest nonzero value $k = \frac{2\pi}{L_3}$ (largest wavelength) to pure red for $k = \frac{2\pi n}{L_3}$. Semitransparent colored regions show the range of short-scale oscillations of $I^{E,B}_{k,R/L}(t)$, and thick solid lines show the time dependence of the time-smeared energies $\bar{I}_{k,R/L}(t)$ defined in (25). Horizontal green lines show the initial energies that are equal for all helical components of electric and magnetic fields.

From Fig. 8 we see that in some simulations (parameter sets number 3–7) the energies of the helical components of the magnetic field exhibit the expected signatures of the inverse cascade due to chiral plasma instability [3,6,12,46]. Namely, the energy of a single longest-wavelength right-handed helical mode rapidly grows at early times and reaches some saturation limit at late evolution time, whereas the energies of all the other modes decrease with time. As expected from the anomalous Maxwell equations (2) with $\sigma_{\mathrm{CME}} = \mu_A/(2\pi^2)$, increasing μ_A by a factor of 2 (to $\mu_A = 1.5$, parameter set number 3, second row in Fig. 8) results in the growth of two right-handed modes. Comparing the data in Figs. 8 and 5, we conclude that the growth of helical magnetic fields is not necessarily accompanied by the decay of the axial charge, and vice versa (see also Table I for a summary of all simulations). Yet another observation that supports this conclusion is that in simulations on the smallest lattice, for which the axial charge exhibits the most rapid decay, we have not found any signatures of the growing electromagnetic fields. Interestingly, increasing the value of μ_A and/or the number of initially excited electromagnetic field modes also does not necessarily speed up the inverse cascade and the decay of Q_A.

An even more interesting picture emerges if we also consider the energies of the helical components of electric fields, shown on Fig. 9. It turns out that for some simulation parameters the long-wavelength helical components of the electric field, rather than the magnetic field, are enhanced during the evolution (parameter sets number 1, 2, and 8). For parameter set number 3, both magnetic and electric fields grow in time. It is remarkable that precisely for these parameter sets the axial charge exhibits the most rapid decay. It seems that both the growth of the helical electric fields and the decay of the axial charge are triggered by sufficiently large initial amplitudes of electromagnetic fields. Thus, it seems that the roles of electric and magnetic fields in the chiral plasma instability scenario are essentially different, in contrast to the simple solution (4) of the anomalous Maxwell equations. It is also interesting to note that we observe the maximal growth of long-wavelength helical electric fields in simulations with a smaller value of Fermi velocity $v_F = 0.75$ (parameter set number 8). Such a strong dependence on the Fermi velocity calls for a proper theoretical analysis.

In order to quantify the net transfer of energy due to the inverse cascade, we follow [46] and introduce the magnetic and electric correlation lengths $\xi_B(t)$ and $\xi_E(t)$ as

$$\xi_{E,B}(t) = \frac{\sum_k \frac{2\pi}{k} I^{E,B}_k(t)}{\sum_k I^{E,B}_k(t)}, \tag{26}$$

where $I^{E,B}_k(t) = I^{E,B}_{k,R}(t) + I^{E,B}_{k,L}(t)$. The time dependence of $\xi_E(t)$ and $\xi_B(t)$, shown on Fig. 10, quantifies the direction of the transfer of energy between short- and long-wavelength modes. $\xi_B(t)$ and $\xi_E(t)$ can also be thought of as the average wavelengths of magnetic and electric fields at a given moment of time. The data shown in Fig. 10 indicate that ξ_E and ξ_B on average increase with time practically for all our simulations, thus providing more quantitative evidence for the inverse cascade. The growth is somewhat more pronounced for the electric correlation length ξ_E, especially in simulations with larger initial amplitude $f = 0.2$. At late evolution times, ξ_E saturates at its upper bound $\xi_E = L_3$ equal to the lattice size. In contrast, the magnetic correlation length ξ_B exhibits rapid growth only at early times, and later seems to saturate at values smaller than L_3. In Fig. 10 we do not show the data for the parameter set number 9, since in this case we have found that only a single initially excited mode strongly dominates the spectrum throughout the whole evolution process, and the quantities ξ_E and ξ_B are trivially equal to L_3 up to some very small corrections.

The effect of saturation of $\xi_{E,B}$ at late evolution times prevents us from checking the universal late-time behavior $\xi_{E,B} \sim \sqrt{t}$ that follows from the scaling analysis of the anomalous Maxwell equations [12,46], similarly to (21). It seems, however, that the late-time behavior of ξ_E is more similar to $\sqrt{t}$ than that of ξ_B.

So far almost all theoretical studies of the chiral plasma instability assume that the axial charge is distributed homogeneously in space and can be described by a coordinate-independent chiral chemical potential μ_A at all evolution times. The extension of the anomalous Maxwell equations (2), which allows us to consider spatially inhomogeneous distributions of axial charge density, has been constructed only recently in [26]. It is thus interesting to check how well the assumption of spatial homogeneity of the axial charge density q_{Ax} holds in our simulations. In order to quantify the spatial inhomogeneity of q_{Ax}, we consider the space-averaged squared deviation of q_{Ax} from its space-averaged value Q_A/V,

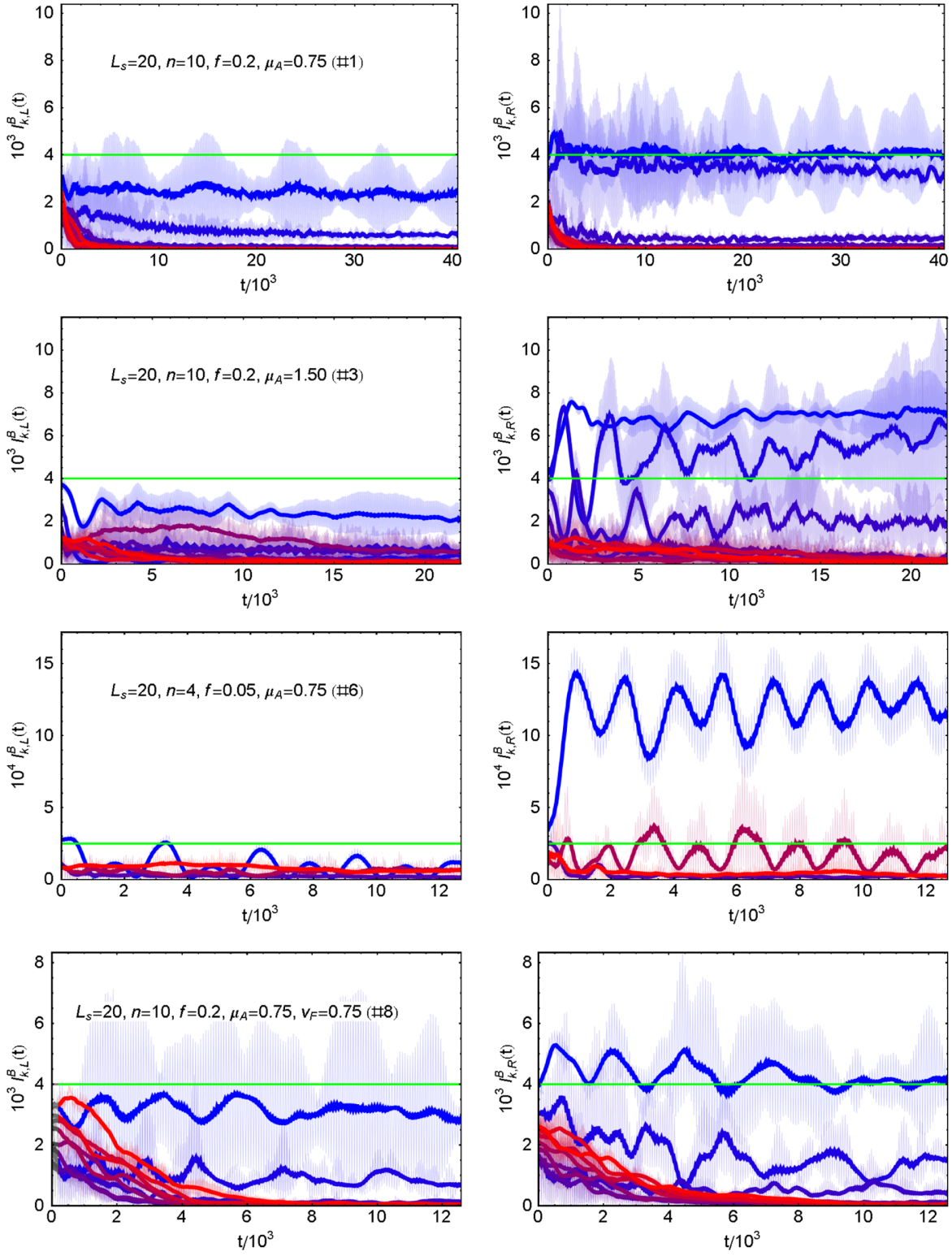

FIG. 8. Time dependence of the energies of helical magnetic fields for several selected sets of simulation parameters. The wave numbers are coded in color, from pure blue for the smallest nonzero value $k = \frac{2\pi}{L_3}$ (largest wavelength) to pure red for $k = \frac{2\pi n}{L_3}$. Semitransparent colored regions show the range of short-scale oscillations of $I^B_{k,R/L}(t)$, and thick solid lines show the time dependence of the time-smeared energies $\bar{I}^B_{k,R/L}(t)$ defined in (25). In the black-and-white version pure blue and pure red correspond to black and light grey, respectively. Horizontal green (light grey) lines show the initial energies, which are equal for all modes. Left-handed and right-handed modes are in the left and in the right columns, respectively.

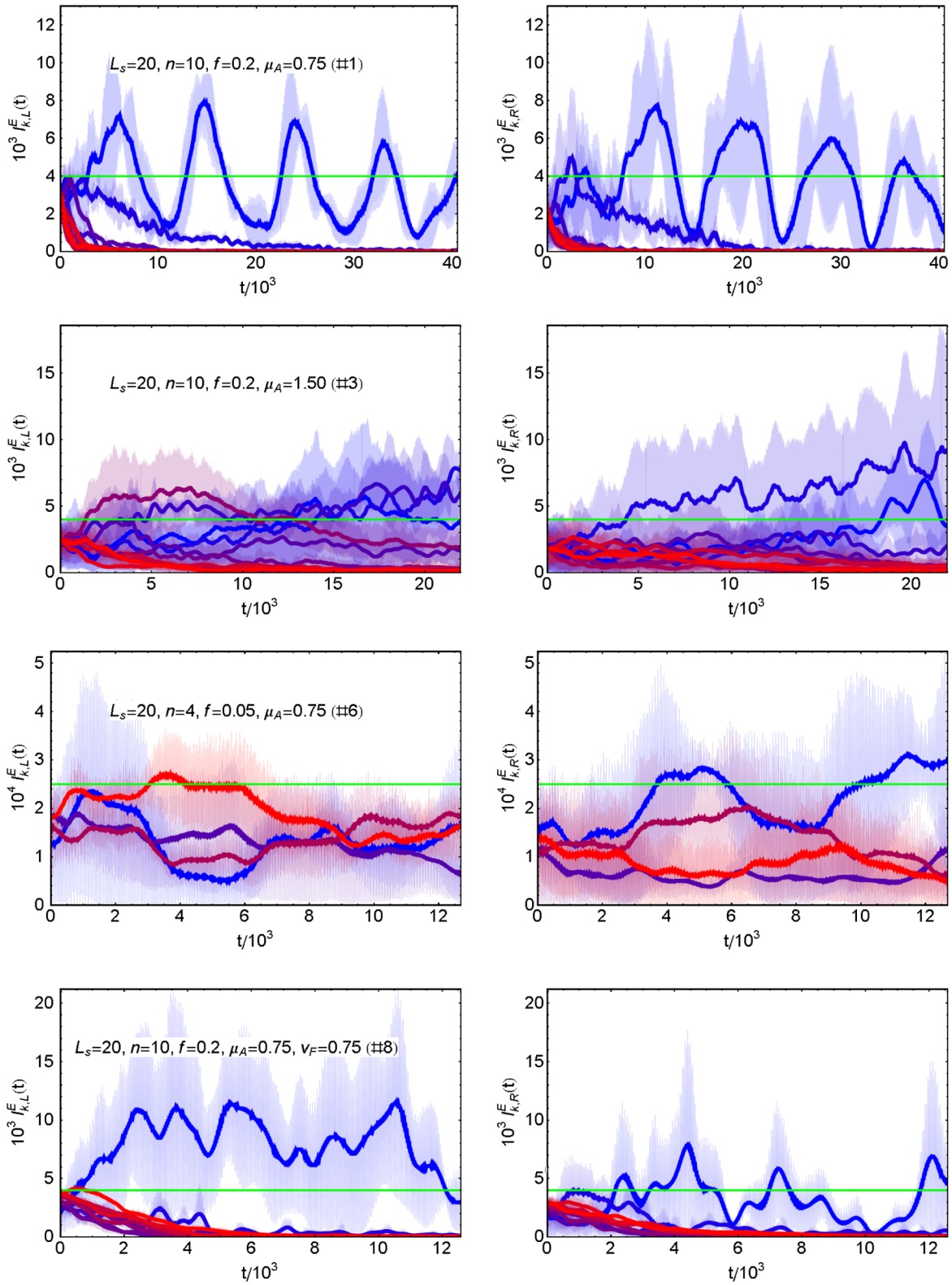

FIG. 9. Time dependence of the energies of helical electric fields for several selected sets of simulation parameters. The wave numbers are coded in color, from pure blue for the smallest nonzero value $k = \frac{2\pi}{L_3}$ (largest wavelength) to pure red for $k = \frac{2\pi n}{L_3}$. Semitransparent colored regions show the range of short-scale oscillations of $I^E_{k,R/L}(t)$, and thick solid lines show the time dependence of the time-smeared energies $\bar{I}^E_{k,R/L}(t)$ defined in (25). In the black-and-white version pure blue and pure red correspond to black and light grey, respectively. Horizontal green (light grey) lines show the initial energies, which are equal for all modes. Left-handed and right-handed modes are in the left and in the right columns, respectively.

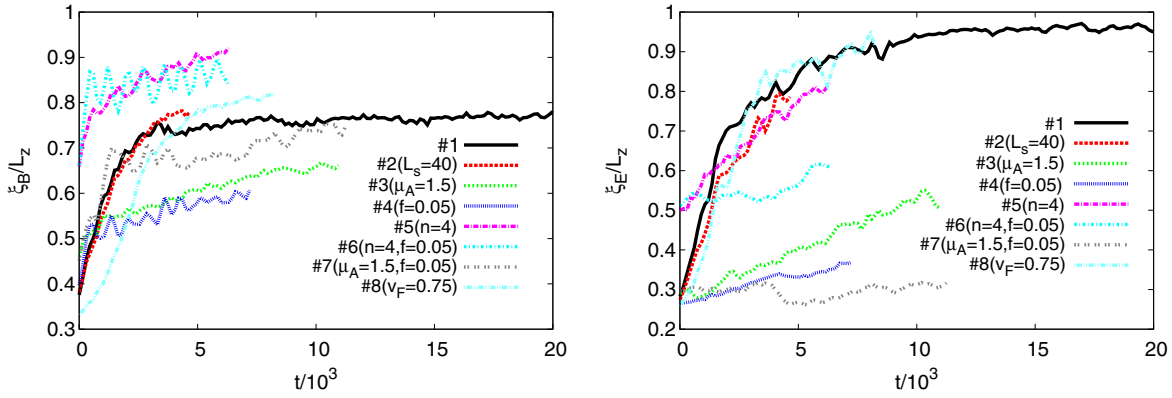

FIG. 10. Magnetic and electric correlation lengths ξ_B and ξ_E [defined in (26)] as functions of time for different parameter sets. A smearing procedure similar to (25) was applied in order to suppress minor short-scale fluctuations in the data.

$$\sigma[q_A] = \sqrt{\sum_x (q_{Ax} - Q_A/V)^2}. \tag{27}$$

The time dependence of the ratio $\sigma[q_A]/(Q_A/V)$ is shown in Fig. 11 for those sets of simulation parameters that exhibit axial charge decay (in particular, this fixes $f = 0.2$).

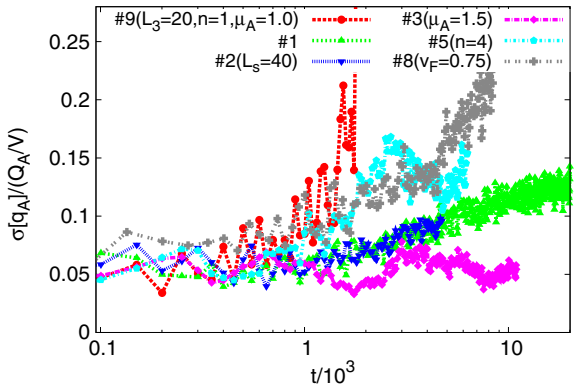

FIG. 11. Time dependence of the standard deviation of the axial charge density $\sigma[q_A]$ from its volume-averaged value Q_A/V in simulations with $f = 0.2$.

Since the Hamiltonian that we use to define the initial state of our simulations involves the initial spatially inhomogeneous configuration A_0 of the vector potential, even at the start of the evolution the axial charge density is slightly inhomogeneous, with deviations from the mean value being of the order of 5%. As one can see from Fig. 11, at late evolution times the inhomogeneity of q_{xA} tends to slightly increase; however, this increase is not dramatic and does not exceed 20%. This suggests that the approximation of spatially homogeneous axial charge distribution is not unreasonable even when the long-wavelength modes are strongly enhanced and dominate the evolution. For simulations with $f = 0.05$ that do not exhibit the decay of the axial charge, the inhomogeneities of the axial charge density remain approximately constant or even tend to decrease.

An interesting question is also the net transfer of energy between fermions and electromagnetic fields. As discussed in Sec. II, in the classical statistical field theory algorithm the total energy of fermions and electromagnetic fields is conserved up to the work performed by the external current (see Fig. 14 in Appendix A for a numerical demonstration). Since in the simulations of chiral plasma instability

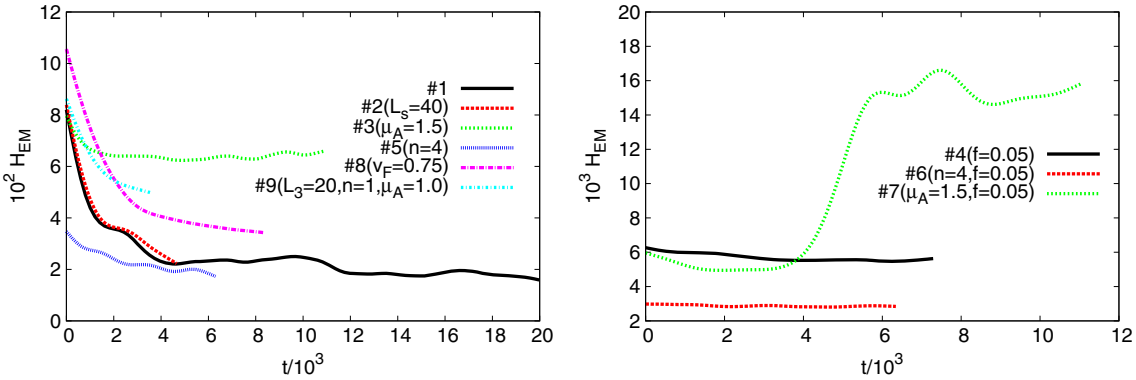

FIG. 12. Time dependence of the total energy of the electromagnetic field in simulations with $f = 0.2$ (on the left) and $f = 0.05$ (on the right). A smearing procedure similar to (25) was applied in order to suppress minor short-scale fluctuations in the data.

discussed in this section the external currents are absent, the transfer of energy can be characterized by the time dependence of the energy of the electromagnetic field alone, which is illustrated in Fig. 12. We see that in almost all simulations the energy of the electromagnetic field decreases or stays constant. The only exception is the simulation with parameter set number 7 ($n = 10$, $f = 0.05$, $\mu_A = 1.5$), for which the energy of the electromagnetic field quickly increases by almost a factor of 3 at $t \gtrsim 6 \cdot 10^3$. Analysis of power spectra suggests that this increase can be at least partly attributed to the enhancement of helical long-wavelength electric fields (similarly to the one observed for parameter set number 3; see the second row in Fig. 9). The decrease of electromagnetic field energy in all the other simulations indicates that it might be not completely correct to think of chiral instability as a "discharge" of an excited state of the Dirac sea into electromagnetic waves.

V. CONCLUSIONS

In this work, we have studied the real-time quantum evolution of chirally imbalanced Wilson-Dirac lattice fermions coupled to the dynamical classical electromagnetic field within the classical statistical field theory approach. The quantum evolution of fermions was simulated exactly (up to small fully controlled errors originating from discretization of time). Our simulations of the chirality pumping process, described by the volume-integrated anomaly equation (5), suggest that the effect of explicit chiral symmetry breaking due to the Wilson term in the lattice Dirac Hamiltonian is not very large. We hope therefore that our results can be confronted at least at the qualitative level with the theoretical predictions for continuum chiral fermions.

We have considered both the generation of chirality imbalance in parallel electric and magnetic fields and the decay of initially present chirality imbalance at the expense of generating electromagnetic fields with nonzero helicity. We have observed that in general the backreaction of dynamical electromagnetic fields prevents fermions from acquiring large chirality imbalance—either by suppression of the chirality pumping or by accelerating the decay of initially present chirality imbalance. The suppression of the chirality pumping process can be understood as the dynamical screening of the external electric field, similarly to what happens in the Schwinger pair creation process [36,38].

In simulations with nonzero initial axial charge Q_A we have also found numerical evidence of the inverse cascade phenomenon due to the chiral plasma instability—that is, rapid growth of long-wavelength magnetic fields of definite helicity at early evolution times and the decay of all other magnetic field components. In some cases, helical electric fields were found to grow, even when magnetic fields did not exhibit any enhancement. A summary of our simulations given in Table I suggests that the growth (or at least the absence of decay) of long-wavelength helical electric fields is a necessary condition for the dynamical decay of the axial charge. The fact that the enhancement of helical electric fields is switched on only for a sufficiently large initial amplitude of the electromagnetic field indicates that nonlinear responses such as the dynamical refringence [55] might be important for the evolution of chirally imbalanced plasma.

We have observed that the mechanism that eventually stops the growth of long-wavelength modes in our simulations is not directly related to the decay of the axial charge. This observation, together with quite different roles of electric and magnetic fields in the evolution process, suggests that the nontrivial momentum and frequency dependence of both the electric conductivity and the chiral magnetic conductivity might be important for the quantitative description of chiral plasma instability. On the other hand, our simulations also indicate that the approximation of the spatially homogeneous axial charge distribution, assumed in most theoretical considerations of anomalous Maxwell equations, is reasonably good even at late evolution times, when the instability has fully developed and the growth of long-wavelength helical electromagnetic fields has saturated.

An interesting further development of our work would be to use chiral lattice fermions in the CSFT algorithm, with the possible choice of the overlap Hamiltonian [56]. In this case, axial charge is conserved in the absence of electromagnetic fields, and the effects of explicit chiral symmetry breaking at high momenta should be absent. Such a setup should be more relevant in the context of high-energy physics, where chiral symmetry tends to be exact at sufficiently high energies (at least at the level of the bare Lagrangian). Yet another interesting open question is the effect of the quantum fluctuations of the electromagnetic field, which are encoded in the nontrivial initial density matrix.

ACKNOWLEDGMENTS

We thank D. Kharzeev, A. Sadofyev, and N. Yamamoto for interesting and stimulating discussions of the physics of chiral media, and F. Hebenstreit and D. Gelfand for useful discussions of the CSFT algorithm. This work was supported by the S. Kowalevskaja award from the Alexander von Humboldt Foundation. We are also indebted to S. Valgushev for his help with code parallelization at the initial stage of this work as well as for the careful reading of this manuscript. The authors are grateful to the FAIR-ITEP supercomputer center where a part of these numerical calculations was performed.

APPENDIX: CLASSICAL STATISTICAL FIELD THEORY ALGORITHM

The starting point of our derivation of the CSFT algorithm is the general expression for the time-dependent expectation value of some quantum operator $\hat{O}$,

$$\langle \hat{O}(t)\rangle = \mathrm{Tr}(\hat{\rho}_0 \hat{U}(t_0,t)\hat{O}\hat{U}^\dagger(t_0,t)), \tag{A1}$$

where $\hat{\rho}_0$ is the initial density matrix and the evolution operator $\hat{U}(t_0,t)$ is the time-ordered exponent

$$\hat{U}(t_0,t) = \mathcal{T}\exp\left(-i\int_{t_0}^{t} dt' \hat{H}(t')\right), \tag{A2}$$

where the Planck constant is set to 1 by an appropriate choice of units. The Hamiltonian operator is defined by Eqs. (6), (7), and (9) in Sec. II. We have allowed for an explicit time dependence of the Hamiltonian, for example, due to the time dependence of the external current $\mathcal{J}_{x,i}(t)$. The evolution operator (A2) can be expanded into a product of elementary evolution operators for small time step $\delta = \frac{t-t_0}{N}$, where δ^{-1} should be much larger than any relevant energy scale in the system,

$$\hat{U}(t,t_0) = \lim_{\delta\to 0}(e^{-i\hat{H}(t_0)\delta}e^{-i\hat{H}(t_0+\delta)\delta}\ldots e^{-i\hat{H}(t)\delta}). \tag{A3}$$

Let us now insert the decompositions of the identity operator $\hat{I} = \prod_{x,i}\int dA_{x,i}|A_{x,i}\rangle\langle A_{x,i}|$ in the Hilbert space of the electromagnetic field between the infinitesimal factors as well as at the beginning and at the end of the product in (A3) in order to arrive at the path integral representation of the evolution operator (A2). We do this both for the forward and the backward evolution operators $\hat{U}(t_0,t)$ and $\hat{U}^\dagger(t_0,t)$ in (A1). It is convenient to enumerate the gauge fields that enter identity decompositions in the forward evolution operators with the discrete lattice time variable $\tau = 0\ldots N$, and in the backward branch—with $\tau = N+1\ldots 2N+1$. The variable τ is a discrete parametrization of the Keldysh contour going from t_0 to t and back (see Fig. 13 for an illustration). Now we have to express the matrix elements $\langle A^\tau|e^{\mp i\hat{H}(\tau)\delta}|A^{\tau+1}\rangle$ of the elementary evolution operators in terms of the fields A^τ and $A^{\tau+1}$. In the derivation of the CSFT algorithm, it is most convenient to use the approximate expression

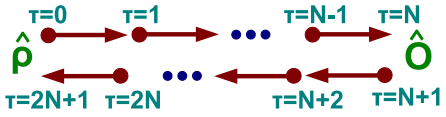

FIG. 13. An illustration of the Schwinger-Keldysh contour with the discrete lattice time τ.

$$\langle A^\tau|e^{-i\hat{H}(\tau)\delta}|A^{\tau+1}\rangle \approx e^{+\frac{i}{2\delta}\sum_{x,i}(A^{\tau+1}_{x,i}-A^{\tau}_{x,i})^2} \times e^{-\frac{i\delta}{2}\sum_{x,i,j}(F^{\tau}_{x,i,j})^2 - i\delta\hat{H}_F[A^\tau] - i\delta\sum_{x,i}A^{\tau}_{x,i}\mathcal{J}^{\tau}_{x,i}} \tag{A4}$$

for the forward evolution operators, and the different approximate expression

$$\langle A^\tau|e^{+i\hat{H}(\tau)\delta}|A^{\tau+1}\rangle \approx e^{-\frac{i}{2\delta}\sum_{x,i}(A^{\tau+1}_{x,i}-A^{\tau}_{x,i})^2} \times e^{+\frac{i\delta}{2}\sum_{x,i,j}(F^{\tau+1}_{x,ij})^2 + i\delta\hat{H}_F[A^{\tau+1}]} + i\delta\sum_{x,i}A^{\tau+1}_{x,i}\mathcal{J}^{\tau+1}_{x,i} \tag{A5}$$

for the backward evolution operators. In the first expression (A4), we order the electromagnetic field operators $\hat{E}_{x,i}$ and $\hat{A}_{x,i}$ in such a way that all the operators in the exponent containing $\hat{A}_{x,i}$ act on the vector $\langle A^\tau|$. In the second expression (A5), these operators act on the vector $|A^{\tau+1}\rangle$. These approximations are both valid to order $O(\delta)$ and differ only in the terms of order $O(\delta^2)$, hence being equivalent in the limit $\delta\to 0$.

Using (A4) and (A5), we arrive at the path integral representation of the expectation value $\langle\hat{O}(t)\rangle$, in which we integrate over the gauge fields living on the discretized Keldysh contour,

$$\begin{aligned}\langle\hat{O}(t)\rangle = \int dA^0\ldots dA^{2N+1}\rho_{\mathrm{EM}}[A^0,A^{2N+1}] \times \mathrm{Tr}(\hat{\rho}_F e^{+\frac{i}{2\delta}\sum_{x,i}(A^1_{x,i}-A^0_{x,i})^2} e^{-i\delta\hat{H}_F[A^0]} e^{-\frac{i\delta}{2}\sum_{x,i,j}(F^0_{x,ij})^2 - i\delta\sum_{x,i}A^0_{x,i}\mathcal{J}^0_{x,i}} \\ \times \ldots\ldots \times e^{+\frac{i}{2\delta}\sum_{x,i}(A^N_{x,i}-A^{N-1}_{x,i})^2} e^{-i\delta\hat{H}_F[A_{N-1}]} e^{-\frac{i\delta}{2}\sum_{x,i,j}(F^{N-1}_{x,ij})^2 - i\delta\sum_{x,i}A^{N-1}_{x,i}\mathcal{J}^{N-1}_{x,i}} \hat{O}[A^N,A^{N+1}] \\ \times e^{-\frac{i}{2\delta}\sum_{x,i}(A^{N+2}_{x,i}-A^{N+1}_{x,i})^2} e^{i\delta\hat{H}_F[A^{N+2}]} e^{\frac{i\delta}{2}\sum_{x,i,j}(F^{N+2}_{x,ij})^2 + i\delta\sum_{x,i}A^{N+2}_{x,i}\mathcal{J}^{N-1}_{x,i}} \\ \times \ldots\ldots \times e^{-\frac{i}{2\delta}\sum_{x,i}(A^{2N+1}_{x,i}-A^{2N}_{x,i})^2} e^{i\delta\hat{H}_F[A^{2N+1}]} e^{\frac{i\delta}{2}\sum_{x,i,j}(F^{2N+1}_{x,ij})^2 + i\delta\sum_{x,i}A^{2N+1}_{x,i}\mathcal{J}^{0}_{x,i}}).\end{aligned} \tag{A6}$$

It is important to stress that at this point we have used the path integral representation only for the bosonic fields, and the exponential factors $e^{\pm i\delta\hat{H}_F[A^\tau]}$ in (A6) are still operators in the fermionic many-body Hilbert space. Correspondingly, the trace in (A6) is taken over this Hilbert space. The operator of the observable $\hat{O}[A^N,A^{N+1}] = \langle A^N|\hat{O}|A^{N+1}\rangle$ is also an operator on the fermionic Hilbert space that depends on fields A^N and A^{N+1}. In deriving the above path integral representation, we have made a simplifying assumption [38] that the initial density matrix $\hat{\rho}_0$ factorizes into the direct product of the fermionic density matrix $\hat{\rho}_F$ (which might in general be

correlated with the initial state of the electromagnetic field) and the density matrix $\hat{\rho}_{\mathrm{EM}}$ of the electromagnetic field with matrix elements $\rho_{\mathrm{EM}}(A^0, A^{2N+1}) = \langle A^0|\hat{\rho}_{\mathrm{EM}}|A^{2N+1}\rangle$. While this assumption is certainly not valid, say, for the density matrix $\hat{\rho} = e^{-\hat{H}/T}$ describing the thermal equilibrium state of the full Hamiltonian $\hat{H}_{\mathrm{EM}} + \hat{H}_F$, it is still justifiable in the case of almost classical dynamics of electromagnetic fields.

At this point let us assume that the observable operator $\hat{O}[A^N, A^{N+1}]$ can be represented as a sum of the identity operator in fermionic Hilbert space (this summand corresponds to purely bosonic observables) and of all possible fermionic bilinear operators,

$$\hat{O}(A^N, A^{N+1}) = O_B(A^N, A^{N+1})\hat{I} + \sum_{x,y}\hat{\psi}^\dagger_x[O_F(A^N, A^{N+1})]_{x,y}\hat{\psi}_y. \quad \text{(A7)}$$

This form is sufficiently general to describe all the observables that we consider in this work. Furthermore, let us assume that the fermionic density matrix $\hat{\rho}_F$ can be represented as an exponent of some fermionic bilinear operator $\hat{H}_0 = \sum_{x,y}\hat{\psi}^\dagger_x[h_0]_{x,y}\hat{\psi}_y$,

$$\hat{\rho}_F = \mathcal{Z}^{-1}\exp(-\hat{H}_0/T), \quad \text{(A8)}$$

where T is some (perhaps fictitious) temperature. Note that in the case of evolution that starts from the nonequilibrium state the operator $\hat{H}_0$ can be different from the Wilson-Dirac Hamiltonian $\hat{H}_F$ that governs the quantum evolution. For instance, the excited state with initial chiral imbalance considered in Sec. IV corresponds to the following form of h_0 in the limit $T \to 0$:

$$h_0 = h[A^0] + \mu_A\sum_a |\psi_a\rangle \mathrm{sign}(\langle\psi_a|\gamma_5|\psi_a\rangle)\langle\psi_a|, \quad \text{(A9)}$$

where $|\psi_a\rangle$ are the eigenstates of the Wilson-Dirac Hamiltonian (7) with the initial gauge field A_0. It is obvious that for the exactly chiral Dirac Hamiltonian with $\langle\psi_a|\gamma_5|\psi\rangle_a = \pm 1$ this definition reduces to the form $h_0 = h + \mu_A\gamma_5$.

Now we are in the position to further simplify the trace over the many-body fermionic Hilbert space in (A6). To this end we use the identities

$$\mathrm{Tr}(e^{\hat{B}_1}\ldots e^{\hat{B}_n}) = \det(1 + e^{B_1}\ldots e^{B_n}), \quad \text{(A10)}$$

$$\mathrm{Tr}(e^{\hat{B}_1}\ldots e^{\hat{B}_n}\hat{O}_F) = \det(1 + e^{B_1}\ldots e^{B_n}) \times \mathrm{Tr}((1 + e^{-B_n}\ldots e^{-B_1})^{-1}O_F), \quad \text{(A11)}$$

where the operators $\hat{B}_i = \sum_{x,y}\hat{\psi}^\dagger_x[B_i]_{x,y}\hat{\psi}_y$ and $\hat{O}_F = \sum_{x,y}\hat{\psi}^\dagger_x O_{x,y}\hat{\psi}_y$ are the fermionic bilinear operators, and the corresponding symbols without hats denote operators on the single-particle fermionic Hilbert space with matrix elements $[B_i]_{x,y}$ and $O_{Fx,y}$. Correspondingly, on the left-hand side the traces are over the many-body fermionic Hilbert space, and the determinants and traces on the right-hand side are on the single-particle fermionic Hilbert space.

As yet another preliminary step in the derivation of the CSFT algorithm, let us also decompose the gauge fields on the forward and the backward branches of the Keldysh contour into the classical gauge field $\overline{A}^\tau_{x,i}$ and the quantum gauge field $\tilde{A}^\tau_{x,i}$ as

$$A^\tau_{x,i} = \overline{A}^\tau_{x,i} + \frac{1}{2}\tilde{A}^\tau_{x,i},$$
$$A^{2N+1-\tau}_{x,i} = \overline{A}^\tau_{x,i} - \frac{1}{2}\tilde{A}^\tau_{x,i}, \qquad \tau = 0\ldots N. \quad \text{(A12)}$$

Relying on the assumptions (A7) and (A8) and using the identities (A10) and (A11), one can rewrite the expression (A6) in terms of the operators on the single-particle fermionic Hilbert space and the variables $\overline{A}^\tau_{x,i}$ and $\tilde{A}^\tau_{x,i}$,

$$\langle\hat{O}(t)\rangle = \mathcal{Z}^{-1}\int d\overline{A}^0\ldots d\overline{A}^N\int d\tilde{A}^0\ldots d\tilde{A}^N\rho_{\mathrm{EM}}\left(\overline{A}^0 + \frac{\tilde{A}^0}{2}, \overline{A}^0 - \frac{\tilde{A}^0}{2}\right)\exp(\mathrm{Tr}\ln(1 + u_-e^{-h_0/T}u_+))$$
$$\times\exp\left(\frac{i}{\delta}\sum_{\tau=0}^{N-1}\sum_{x,i}(\tilde{A}^{\tau+1}_{x,i} - \tilde{A}^\tau_{x,i})(\overline{A}^{\tau+1}_{x,i} - \overline{A}^\tau_{x,i}) - i\delta\sum_{\tau=0}^{N-1}\sum_{x,i}\tilde{A}^\tau_{x,i}\left(\mathcal{J}^\tau_{x,i} + \sum_j\overline{F}^\tau_{x,i,j} - \overline{F}^\tau_{x-\hat{j},i,j}\right)\right)$$
$$\times\left(O_0\left(\overline{A}^N + \frac{\tilde{A}^N}{2}, \overline{A}^N - \frac{\tilde{A}^N}{2}\right) + \mathrm{Tr}\left((1 + u_+^{-1}e^{+h_0/T}u_-^{-1})^{-1}O_1\left(\overline{A}^N + \frac{\tilde{A}^N}{2}, \overline{A}^N - \frac{\tilde{A}^N}{2}\right)\right)\right), \quad \text{(A13)}$$

where the field strength tensor $\overline{F}^\tau_{x,ij}$ is constructed from the classical component of the gauge field $\overline{A}^\tau_{x,i}$ exactly in the same way as in (10) and we have introduced the unitary single-particle forward and backward evolution operators,

$$u_+ = e^{-i\delta h[\overline{A}^0+\frac{\tilde{A}^0}{2}]}\ldots e^{-i\delta h[\overline{A}^{N-1}+\frac{\tilde{A}^{N-1}}{2}]},$$
$$u_- = e^{+i\delta h[\overline{A}^{N-1}-\frac{\tilde{A}^{N-1}}{2}]}\ldots e^{+i\delta h[\overline{A}^0-\frac{\tilde{A}^0}{2}]}. \quad \text{(A14)}$$

The path integral representation (A6) is exact in the limit $N\to\infty$, $\delta\to 0$ with fixed $t=N\delta$ (up to the simplifying assumptions on the form of the observable operator $\hat{O}$ and the initial density matrix $\hat{\rho}$), but is not suitable for numerical analysis. The key step in the derivation of the CSFT algorithm is to expand the fermion-induced effective action of the electromagnetic field $S_F=\mathrm{Tr}\ln(1+u_-e^{-h_0/T}u_+)$ in the first line of (A13) to the linear order in the quantum electromagnetic field $\tilde{A}_{x,i}$,

$$S_F \approx S_F|_{\tilde{A}^\tau_{x,i}=0} + \sum_{\tau=0}^{N}\sum_{x,i}\tilde{A}^\tau_{x,i}\frac{\partial}{\partial\tilde{A}^\tau_{x,i}}S_F\bigg|_{\tilde{A}^\tau_{x,i}=0}. \quad \text{(A15)}$$

In order to calculate the first derivative of S_F over $\tilde{A}^\tau_{x,i}$, we use the identities

$$\frac{\partial}{\partial\tilde{A}^\tau_{x,i}}u_+\bigg|_{\tilde{A}^\tau_{x,i}=0} = -\frac{i\delta}{2}u(0,\tau)j[\overline{A}^\tau]u(\tau,N),$$
$$\frac{\partial}{\partial\tilde{A}^\tau_{x,i}}u_-\bigg|_{\tilde{A}^\tau_{x,i}=0} = -\frac{i\delta}{2}u^\dagger(\tau,N)j[\overline{A}^\tau]u^\dagger(0,\tau), \quad \text{(A16)}$$

where we have introduced the single-particle operator of the conserved electric current

$$j_{x,i}[A]=\frac{\partial h[A]}{\partial A_{x,i}} \quad \text{(A17)}$$

as well as the single-particle evolution operator in the background of the classical electromagnetic field $\overline{A}^\tau_{x,i}$,

$$u(\tau_1,\tau_2)=e^{-i\delta h[\overline{A}^{\tau_1}]}\ldots e^{-i\delta h[\overline{A}^{\tau_2-1}]}, \qquad \tau_2\geq\tau_1. \quad \text{(A18)}$$

The identities (A16) are exact up to the order $O(\delta^2)$, since in the derivatives of the forward and backward evolution operators we have used different orderings of the elementary evolution operator $e^{-i\delta h[\overline{A}^\tau]}$ and the current operator $j[\overline{A}^\tau]$.

Using (A16) and the relations $u_+(0,N)|_{\tilde{A}=0}=u(0,N)$ and $u_-(0,N)|_{\tilde{A}=0}=u^\dagger(0,N)$, after some simple algebraic manipulations we can rewrite the derivative over $\tilde{A}^\tau_{x,i}$ in (A15) as

$$\frac{\partial}{\partial\tilde{A}^\tau_{x,i}}S_F\bigg|_{\tilde{A}^\tau_{x,i}=0} \equiv \langle j^\tau_{x,i}\rangle = -i\delta\mathrm{Tr}\left(\frac{1}{1+e^{h_0/T}}u(0,\tau)j_{x,i}[\overline{A}^\tau]u^\dagger(0,\tau)\right). \quad \text{(A19)}$$

Now that our action (A15) is assumed to be linear in the quantum field $\tilde{A}^\tau_{x,i}$ for $\tau=1\ldots N-1$, the quantum field $\tilde{A}^\tau_{x,i}$ can be integrated out in a straightforward way in the case of purely bosonic observables with $O_F\equiv 0$. The case of fermionic observables with nontrivial $O_F(\overline{A}^N+\frac{\tilde{A}^N}{2},\overline{A}^N-\frac{\tilde{A}^N}{2})$ is more subtle, since in the path integral representation (A13) the fermionic observable itself depends on $\tilde{A}^\tau_{x,i}$ [via the factor $(1+u_+^{-1}e^{+h_0/T}u_-^{-1})^{-1}$ under the fermionic trace in the last line of (A13)]. It is a common assumption in the derivation of the CSFT algorithm to neglect the $\tilde{A}^\tau_{x,i}$ dependence of the fermionic observables (see, e.g., [38]), which can be justified, e.g., if the relevant physical processes involve a large number of virtual fermionic particles. In this case one can argue that the exponent of the effective action S_F has a much stronger dependence on $\tilde{A}^\tau_{x,i}$ than the observable. A heuristic argument in favor of such an assumption is that if one neglects the $\tilde{A}^\tau_{x,i}$ dependence of the fermionic observables, the expectation values of all fermionic bilinear operators take exactly the same form as the expectation values of the electric current (A19) and the fermionic energy [see Eq. (15) below]. Since these quantities are related to the observables characterizing the classical electromagnetic field via the inhomogeneous Maxwell equations and the energy conservation law, they are certainly also physical observables. While the $\tilde{A}^\tau$ dependence of the observable operator might still encode some interesting effects of the backreaction of measurements on the quantum evolution, taking it into account would presumably lead to a significant complication of the CSFT algorithm. For all these reasons, we also assume that the factor $(1+u_+^{-1}e^{+h_0/T}u_-^{-1})^{-1}$ in (A13) depends negligibly weakly on $\tilde{A}^\tau$ and replace it by $(1+u^{-1}(0,N)e^{+h_0/T}u(0,N)^{\dagger-1})^{-1}$.

In order to integrate out the fields $\tilde{A}^0_{x,i}$ and $\tilde{A}^N_{x,i}$ at the end points of the Keldysh contour, it is convenient to introduce the Wigner transforms $\overline{\rho}_{\mathrm{EM}}(\overline{A}^0_{x,i},\overline{E}^0_{x,i})$ and $\overline{O}_{1,2}(\overline{A}^N_{x,i},\overline{E}^N_{x,i})$ of the initial density matrix $\hat{\rho}_{\mathrm{EM}}$ and the operators $O_{F,B}$ in (A7),

$$\rho_{\mathrm{EM}}\left(\overline{A}^0+\frac{\tilde{A}^0}{2},\overline{A}^0-\frac{\tilde{A}^0}{2}\right) = \int d\overline{E}^0_{x,i}\overline{\rho}_{\mathrm{EM}}(\overline{A}^0_{x,i},\overline{E}^0_{x,i})e^{i\sum_{x,i}\overline{E}^0_{x,i}\tilde{A}^0_{x,i}} \quad \text{(A20)}$$

$$O_{F,B}\left(\overline{A}^N+\frac{\tilde{A}^N}{2},\overline{A}^N-\frac{\tilde{A}^N}{2}\right) = \int d\overline{E}^N_{x,i}\overline{O}_{F,B}(\overline{A}^N_{x,i},\overline{E}^N_{x,i})e^{-i\sum_{x,i}\overline{E}^N_{x,i}\tilde{A}^N_{x,i}}, \quad \text{(A21)}$$

where $\overline{E}^\tau_{x,i}$ is the classical electric field. We also note that the first sum over τ in the second line of (A13) can be rewritten as

$$\sum_{\tau=0}^{N-1}\sum_{x,i}(\tilde{A}^{\tau+1}_{x,i}-\tilde{A}^{\tau}_{x,i})(\overline{A}^{\tau+1}_{x,i}-\overline{A}^{\tau}_{x,i})=-\sum_{\tau=1}^{N-1}\sum_{x,i}\tilde{A}^{\tau}_{x,i}(\overline{A}^{\tau+1}_{x,i}+\overline{A}^{\tau-1}_{x,i}-2\overline{A}^{\tau}_{x,i})+\sum_{x,i}(\tilde{A}^{N}_{x,i}(\overline{A}^{N}_{x,i}-\overline{A}^{N-1}_{x,i})-\tilde{A}^{0}_{x,i}(\overline{A}^{1}_{x,i}-\overline{A}^{0}_{x,i})). \tag{A22}$$

Finally, we are ready to integrate out the quantum electromagnetic field $\tilde{A}^{\tau}_{x,i}$, which leads to the following expression for the expectation value $\langle\hat{O}(t)\rangle$:

$$\begin{aligned}\langle\hat{O}(t)\rangle=&\int d\overline{E}^0 d\overline{E}^N\int d\overline{A}^0\ldots d\overline{A}^N\tilde{\rho}_{\mathrm{EM}}(\overline{A}^0,\overline{E}^0)\times\delta\left[\overline{E}^0-\frac{\overline{A}^1-\overline{A}^0}{\delta}-\delta\mathcal{R}^0\right]\\&\times\prod_{\tau=1}^{N-1}\delta\left[\frac{\overline{A}^{\tau+1}+\overline{A}^{\tau-1}-2\overline{A}^{\tau}}{\delta}+\delta\mathcal{R}^{\tau}\right]\delta\left[\overline{E}^N-\frac{\overline{A}^N-\overline{A}^{N-1}}{\delta}\right]\\&\times(\overline{O}_0(\overline{A}^N,\overline{E}^N)+\mathrm{Tr}((1+e^{h_0/T})^{-1}u(0,N)\overline{O}_1(\overline{A}^N,\overline{E}^N)u^{\dagger}(0,N))),\end{aligned} \tag{A23}$$

where

$$\mathcal{R}^{\tau}_{x,i}=\mathcal{J}^{\tau}_{x,i}+\langle\hat{j}^{\tau}_{x,i}\rangle+\sum_j(\overline{F}^{\tau}_{x,ij}-\overline{F}^{\tau}_{x-\hat{j},ij}), \tag{A24}$$

and $\langle j^{\tau}_{x,i}\rangle$ is the expectation value of the electric current defined as in (A19). We note that the normalization factor $\mathcal{Z}^{-1}$ in (A8) and (A13) is canceled by the zeroth-order term of the expansion (A15).

From the explicit expression (A19) for the fermionic electric current $\langle j^{\tau}_{x,i}\rangle$ one can immediately see that it depends only on the classical electromagnetic field $\overline{A}^{\tau'}_{x,i}$ with $\tau'<\tau$. Therefore, the delta functions in the integral (A23) can be regarded as the constraints on the deterministic evolution of the classical electromagnetic field $\overline{A}^{\tau}_{x,i}$ interacting with the quantum fermionic field. To make this more obvious, we can rewrite the chain of δ-functions in (A23) as

$$\begin{aligned}&\delta[\overline{A}^1-\mathcal{A}^1[\overline{A}^0,\overline{E}^0]]\prod_{\tau=2}^{N}\delta[\overline{A}^{\tau}-\mathcal{A}^{\tau}[\overline{A}^{\tau-1},\overline{A}^{\tau-2},\langle j^{\tau-1}\rangle]]\delta\left[\overline{E}^N-\frac{\overline{A}^N-\overline{A}^{N-1}}{\delta}\right],\\&\mathcal{A}^1[\overline{A}^0,\overline{E}^0]=\overline{A}^0+\delta(\overline{E}^0-\delta\mathcal{R}^0),\\&\mathcal{A}^{\tau}[\overline{A}^{\tau-1},\overline{A}^{\tau-2},\langle j^{\tau-1}\rangle]=2\overline{A}^{\tau-1}-\overline{A}^{\tau-2}-\delta^2\mathcal{R}^{\tau-1},\end{aligned} \tag{A25}$$

where the last definition is for $\tau=2\ldots N$. From this expression one can see that one can sequentially integrate out the fields $\overline{A}^{\tau}$ with $\tau=1\ldots N-1$ and express the fields $\overline{A}^N$, $\overline{E}^N$ in terms of the initial values $\overline{A}^0$, $\overline{E}^0$. Namely, integrating out the field $\overline{A}^1$ first, we remove the first delta function in the product in (A25) and replace $\overline{A}^1$ by $\mathcal{A}^1[\overline{A}^0,\overline{E}^0]$ in the arguments of all the other delta functions. Integrating out $\overline{A}^2$, we remove the second delta functions and replace $\overline{A}^2$ by $\mathcal{A}^2[\overline{A}^0,\overline{E}^0]\equiv\mathcal{A}^2(\mathcal{A}^1[\overline{A}^0,\overline{E}^0],\overline{A}^0,\langle j^1\rangle)$. We can repeat this process for all τ up to $N-1$, each time expressing $\mathcal{A}^{\tau}$ in terms of the initial values $\overline{A}^0$ and $\overline{E}^0$ and the functionals $\mathcal{A}^{\tau'}$ with $\tau'<\tau$. It is important that in such a sequential integration, the integrand $\overline{A}^{\tau}$ always enters the argument of the delta function being removed linearly. Therefore, despite the nonlinearity of the chain of evolution equations, such intermediate integrations do not produce a nontrivial Jacobian. To our knowledge, the absence of the Jacobian in the integration measure in the CSFT algorithm so far has only been demonstrated for scalar field theory [57,58]. It is nice to see here explicitly its absence for lattice gauge theory coupled to fermions.

After integrating out all the intermediate fields $\overline{A}^{\tau}$ with $\tau=1\ldots N-1$, we are left with the following form of Eq. (A23):

$$\begin{aligned}\langle\hat{O}(t)\rangle=&\int d\overline{A}^0 d\overline{E}^0\int d\overline{A}^N d\overline{E}^N\overline{\rho}_{\mathrm{EM}}(\overline{A}^0,\overline{E}^0)\\&\times\delta[\overline{A}^N-\mathcal{A}^N[\overline{A}^0,\overline{E}^0]]\delta[\overline{E}^N-\mathcal{E}^N[\overline{A}^0,\overline{E}^0]]\\&\times\left(\overline{O}_0(\overline{A}^N,\overline{E}^N)\right.\\&\left.+\mathrm{Tr}\left(\frac{1}{1+e^{h_0/T}}u(0,N)\overline{O}_1(\overline{A}^N,\overline{E}^N)u^{\dagger}(0,N)\right)\right),\end{aligned} \tag{A26}$$

where

$$\mathcal{E}^N[\bar{A}^0,\bar{E}^0]=\frac{\mathcal{A}^N[\bar{A}^0,\bar{E}^0]-\mathcal{A}^{N-1}[\bar{A}^0,\bar{E}^0]}{\delta} \tag{A27}$$

and we have expressed the functionals $\mathcal{A}^N$ and $\mathcal{A}^{N-1}$ in terms of the initial values $\bar{A}^0$, $\bar{E}^0$ of the vector gauge potential and the electric field. In this expression, it is straightforward to integrate out $\bar{A}^N$ and $\bar{E}^N$, which amounts to substituting $\mathcal{A}^N[\bar{A}^0,\bar{E}^0]$ and $\mathcal{E}^N[\bar{A}^0,\bar{E}^0]$ in place of $\bar{A}^N$ and $\bar{E}^N$ in the Wigner transforms of the observable operators O_B and O_F.

To summarize, the CSFT algorithm amounts to a simultaneous time evolution of the classical electromagnetic fields, described by the vector potential $\bar{A}^\tau_{x,i}$ and the electric field $\bar{E}^\tau_{x,i}$, and the quantum fermionic fields, described by single-particle evolution operator $u(0,\tau)$ in (A18). The discrete equations that govern this evolution [arguments of the delta functions in (A23)] have a well-defined continuum limit $\delta\to 0$, $N\to\infty$ with fixed $t=N\delta$, which is given by Eqs. (11)–(13) in the main text. To simplify the notation, in the main part of the text we omit the bar over the classical components of the gauge field and denote them as $A_{x,i}(t)\equiv\bar{A}^\tau_{x,i}$, $E_{x,i}(t)\equiv\bar{E}^\tau_{x,i}$, $F_{x,ij}(t)\equiv\bar{F}^\tau_{x,ij}$.

In practice, however, the numerical solution of the continuum equations (11)–(13) should necessarily involve some discretization of time. While the simple discretization of the Keldysh contour used in the above derivation can be, in principle, used for a numerical solution at sufficiently small δ, for a given finite δ one can construct different, more advanced discretizations that would reduce discretization errors, thus improving the conservation of energy (15) and making the single-particle evolution operator $u(0,\tau)$ numerically closer to a unitary matrix.

In this work we follow [35,38] and use the leapfrog evolution scheme for the single-particle evolution operator $u^\tau\equiv u(0,\tau)$, which significantly improves the conservation of the unitarity condition $u(0,\tau)u^\dagger(0,\tau)=1$ at finite discrete time step δ,

$$\begin{aligned} u^{\tau+1}&=u^{\tau-1}-i\delta h[\bar{A}^\tau]u^\tau, \qquad \tau=1\ldots N-1\\ u^1&=u^0-i\delta h[\bar{A}^0]u^0, \qquad u^0=1. \end{aligned} \tag{A28}$$

In practice it is convenient to work with the components of u^τ in the basis of eigenstates of the initial single-particle Hamiltonian $h[\bar{A}^0]$. In particular, if translational invariance along some of the space directions is preserved during the evolution, u^τ remains block diagonal in the basis of plane waves propagating along these directions. This block-diagonal structure can be used to greatly reduce the number of independent components of u^τ that enter the equations (A28). We have used translational invariance in two out of three spatial lattice directions to speed up the evolution algorithm on large lattices with sizes up to $200\times 40\times 40$, assuming translational invariance in two out of three spatial directions.

For the evolution of the electromagnetic field we use the equations that directly follow from (A23),

$$\begin{aligned} \frac{\bar{E}^{\tau+1}_{x,i}-\bar{E}^\tau_{x,i}}{\delta}&=-\mathcal{J}^\tau_{x,i}-\langle\hat{j}^\tau_{x,i}\rangle-\sum_j(\bar{F}^\tau_{x,ij}-\bar{F}^\tau_{x-\hat{j},ij}),\\ \frac{\bar{A}^{\tau+1}_{x,i}-\bar{A}^\tau_{x,i}}{\delta}&=\bar{E}^{\tau+1}_{x,i},\\ \frac{\bar{A}^1_{x,i}-\bar{A}^0_{x,i}}{\delta}&=\bar{E}^0_{x,i}-\delta\left(\mathcal{J}^0_{x,i}+\langle\hat{j}^0_{x,i}\rangle+\sum_j(\bar{F}^0_{x,ij}-\bar{F}^0_{x-\hat{j},ij})\right). \end{aligned} \tag{A29}$$

In our simulations, we use the value $\delta=0.05$. We have checked that decreasing δ down to 0.02 does not change our results up to some small unimportant fluctuations.

In principle, leapfrog-type time discretization (A28) allows the existence of fermionic doublers in time direction—that is, the symmetric finite differences in (A28) are 0 if the mode functions oscillate as $(-1)^\tau$. Such doubler modes correspond to another flavor of Dirac fermions with an opposite signature of the γ_5 matrix. Thus, if such modes are excited, they can also contribute to the anomaly equation (5) and effectively decrease the anomaly coefficient, or lead to the decay of the initial value of the axial charge [33]. In order to check whether fermionic modes with such high frequencies are excited we have calculated the average norm of forward finite differences of u^τ as $\frac{1}{4V}\mathrm{Tr}((u^{\tau+1}-u^\tau)^\dagger(u^{\tau+1}-u^\tau))$. Since the size of the single-particle Hilbert space is equal to $4V$ this quantity should be of the order of δ^2 if u^τ are smooth functions of τ. On the other hand, doubler modes with $u^\tau\sim(-1)^\tau$ yield the contribution of the order of unity. In our simulations we have checked that the above norm remains of the order of 10^{-2} for all evolution times and does not exhibit any tendency to grow. This suggests that the doubler modes remain practically unexcited during the evolution.

Another important characteristic of the discretization of the evolution equations (11) and (13) is the precision with which the conservation of energy (15) holds. For the leapfrog equations (A28) and (A29) the total energy of electromagnetic fields and fermions is conserved only approximately, up to the terms of the order of δ^2. In order to illustrate the conservation of energy in our simulations, in Fig. 14 we show the time dependence of the fermionic energy $\langle\hat{H}_F\rangle$, the energy H_{EM} of electromagnetic fields, and their total. One can see that while both $\langle\hat{H}_F\rangle$ and H_{EM} change quite significantly during the evolution, their sum is conserved with very good precision, which again shows that the time step $\delta=0.05$ is small enough.

The discrete evolution equations (A28) and (A29) are ideally suited for parallelization on multinode computers. Indeed, the largest amount of computer time is required to

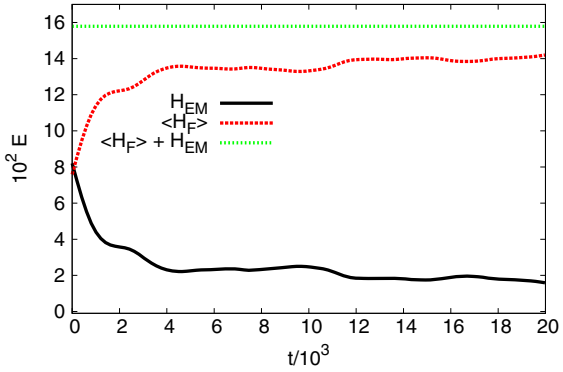

FIG. 14. Time dependence of the energies of fermions and electromagnetic fields and their total for simulations on a $200 \times 20 \times 20$ lattice with $n = 10$, $f = 0.2$, $\mu_A = 0.75$, $v_F = 1$ (parameter set number 1 in Table I).

solve the evolution equation (A28) for the $(4V) \times (4V)$ matrix u^τ. Taking into account that only half of the single-particle fermionic states is filled at zero temperature, this size can be reduced by a factor of 2 down to $(2V) \times (4V)$. The evolution of the electromagnetic field (A29) requires only the total electric current summed over all fermionic modes, and is computationally very cheap. Thus, it is natural to distribute the rows of the u^τ matrix over multiple nodes. On each node, one performs the elementary evolution step (A28) for the rows attributed to this node and calculates the partial traces of the electric current and other fermionic bilinear operators over these rows. The results are sent to the master node, which calculates the total current and performs the evolution of the electromagnetic field according to (A29). Since the amount of data transferred by the network from each slave node to the master node is significantly smaller than the amount of data stored at each slave mode (for realistic lattice sizes and node numbers, the number of rows of u^τ per node is large), the speed of the algorithm scales practically linearly with the number of slave nodes.

Such parallelization also solves the problem with a very large amount of RAM memory required to store the matrix u^τ (∼36 Gb for the $20 \times 20 \times 20$ lattice when one uses 8-byte double accuracy numbers for all fields), which is simply split over different nodes. In order to further decrease the required RAM size, we use the 4-byte float numbers to store u^τ. We have explicitly checked that the reduction from double to float real numbers practically does not affect our results.

The extensive parallelization also allows us to avoid the stochastic summation over all modes [35–38], which introduces additional statistical noise in the results and can therefore significantly affect potentially unstable evolution, which we study in this work. Instead, we perform exact summation over all initially occupied fermionic states.

[1] M. Joyce and M. Shaposhnikov, Phys. Rev. Lett. **79**, 1193 (1997).
[2] V. B. Semikoz and J. W. F. Valle, J. Cosmol. Astropart. Phys. 11 (2011) 048.
[3] A. Boyarsky, J. Froehlich, and O. Ruchayskiy, Phys. Rev. Lett. **108**, 031301 (2012).
[4] H. Tashiro, T. Vachaspati, and A. Vilenkin, Phys. Rev. D **86**, 105033 (2012).
[5] M. Giovannini, Phys. Rev. D **88**, 063536 (2013).
[6] A. Boyarsky, J. Fröhlich, and O. Ruchayskiy, Phys. Rev. D **92**, 043004 (2015).
[7] G. Sigl and N. Leite, J. Cosmol. Astropart. Phys. 01 (2016) 025.
[8] H. Ooguri and M. Oshikawa, Phys. Rev. Lett. **108**, 161803 (2012).
[9] Q. Li, D. E. Kharzeev, C. Zhang, Y. Huang, I. Pletikosic, A. V. Fedorov, R. D. Zhong, J. A. Schneeloch, G. D. Gu, and T. Valla, Nat. Phys. **12**, 550 (2016).
[10] H. J. Kim, K. S. Kim, J. F. Wang, M. Sasaki, N. Satoh, A. Ohnishi, M. Kitaura, M. Yang, and L. Li, Phys. Rev. Lett. **111**, 246603 (2013).
[11] J. Xiong, S. K. Kushwaha, T. Liang, J. W. Krizan, W. Wang, R. J. Cava, and N. P. Ong, arXiv:1503.08179.
[12] Y. Hirono, D. Kharzeev, and Y. Yin, Phys. Rev. D **92**, 125031 (2015).
[13] Y. Akamatsu and N. Yamamoto, Phys. Rev. Lett. **111**, 052002 (2013).
[14] C. Manuel and J. M. Torres-Rincon, Phys. Rev. D **92**, 074018 (2015).
[15] K. Tuchin, Phys. Rev. C **91**, 064902 (2015).
[16] K. Fukushima, D. E. Kharzeev, and H. J. Warringa, Phys. Rev. D **78**, 074033 (2008).
[17] D. E. Kharzeev and H. J. Warringa, Phys. Rev. D **80**, 034028 (2009).
[18] D. Hou, H. Liu, and H. Ren, J. High Energy Phys. 05 (2011) 046.
[19] D. Satow and H. Yee, Phys. Rev. D **90**, 014027 (2014).
[20] P. V. Buividovich, Nucl. Phys. **A925**, 218 (2014).
[21] I. Amado, K. Landsteiner, and F. Pena-Benitez, J. High Energy Phys. 05 (2011) 081.
[22] K. Landsteiner, E. Megias, and F. Pena-Benitez, *Lecture Notes in Physics: Strongly interacting matter in magnetic fields*, edited by D. Kharzeev, K. Landsteiner, A. Schmitt, and H.-U. Yee (Springer, New York, 2012).
[23] P. V. Buividovich, M. Puhr, and S. N. Valgushev, Phys. Rev. B **92**, 205122 (2015).

[24] C. Manuel and J. M. Torres-Rincon, Phys. Rev. D **89**, 096002 (2014).
[25] C. Manuel and J. M. Torres-Rincon, Phys. Rev. D **90**, 076007 (2014).
[26] E. V. Gorbar, I. A. Shovkovy, S. Vilchinskii, I. Rudenok, A. Boyarsky, and O. Ruchayskiy, Phys. Rev. D **93**, 105028 (2016).
[27] It is interesting that nonzero scalar product $\vec{E} \cdot \vec{B}$ is only possible for exponentially growing or decaying solutions, e.g., circularly polarized electromagnetic waves in a dissipationless medium always have $\vec{E} \cdot \vec{B} = 0$.
[28] Z. V. Khaidukov, V. P. Kirilin, A. V. Sadofyev, and V. I. Zakharov, arXiv:1307.0138.
[29] V. P. Kirilin, A. V. Sadofyev, and V. I. Zakharov, arXiv:1312.0895.
[30] M. A. Stephanov and Y. Yin, Phys. Rev. Lett. **109**, 162001 (2012).
[31] D. T. Son and P. Surowka, Phys. Rev. Lett. **103**, 191601 (2009).
[32] Y. Akamatsu, A. Rothkopf, and N. Yamamoto, J. High Energy Phys. 03 (2016) 210.
[33] G. Aarts and J. Smit, Nucl. Phys. **B555**, 355 (1999).
[34] G. Aarts and J. Smit, Phys. Rev. D **61**, 025002 (1999).
[35] S. Borsanyi and M. Hindmarsh, Phys. Rev. D **79**, 065010 (2009).
[36] F. Gelis and N. Tanji, Phys. Rev. D **87**, 125035 (2013).
[37] J. Berges, D. Gelfand, and D. Sexty, Phys. Rev. D **89**, 025001 (2014).
[38] V. Kasper, F. Hebenstreit, and J. Berges, Phys. Rev. D **90**, 025016 (2014).
[39] K. Fukushima, Phys. Rev. D **92**, 054009 (2015).
[40] A. M. Polyakov, Phys. Lett. B **59**, 82 (1975).
[41] M. M. Vazifeh and M. Franz, Phys. Rev. Lett. **111**, 027201 (2013).
[42] P. Hosur and X. Qi, Comp. Rend. Phys. **14**, 857 (2013).
[43] A. Sekine and K. Nomura, J. Phys. Soc. Jpn. **83**, 094710 (2014).
[44] N. Tanji, N. Mueller, and J. Berges, Phys. Rev. D **93**, 074507 (2016).
[45] S. A. Parameswaran, T. Grover, D. A. Abanin, D. A. Pesin, and A. Vishwanath, Phys. Rev. X **4**, 031035 (2014).
[46] N. Yamamoto, Phys. Rev. D **93**, 125016 (2016).
[47] This of course requires that the initial density matrix should correspond to a sufficiently classical state, so that the Wigner transform of the initial density matrix is nonnegative.
[48] In the process of developing our algorithm we reproduced the results of [38] on the Schwinger pair production with massive fermions and explicitly checked that initial quantum fluctuations of the electromagnetic field encoded in the nontrivial initial density matrix $\hat{\rho}_{\mathrm{EM}} \sim e^{-\hat{H}_{\mathrm{EM}}/T}$ with $T \to 0$ (so that only the ground state energies $\hbar w/2$ contribute) have little effect on the Schwinger pair production rate. Correspondingly, only a few samples of A_0 and E_0 are enough for reliably computing the expectation values.
[49] S. L. Adler, arXiv:hep-ph/0405040.
[50] A. A. Anselm and A. A. Iogansen, JETP Lett. **49**, 214 (1989).
[51] K. Jensen, P. Kovtun, and A. Ritz, J. High Energy Phys. 10 (2013) 186.
[52] L. H. Karsten and J. Smith, Nucl. Phys. **B183**, 103 (1981).
[53] H. J. Rothe and N. Sadooghi, Phys. Rev. D **58**, 074502 (1998).
[54] M. H. Al-Hashimi and U. Wiese, Ann. Phys. (Amsterdam) **324**, 343 (2009).
[55] N. Mueller, F. Hebenstreit, and J. Berges, arXiv:1605.01413.
[56] M. Creutz, I. Horvath, and H. Neuberger, Nucl. Phys. B, Proc. Suppl. **106–107**, 760 (2002).
[57] S. Jeon, Phys. Rev. C **72**, 014907 (2005).
[58] E. Gozzi and M. Regini, Phys. Rev. D **62**, 067702 (2000).